Journal of Asian Earth Sciences 140 (2017) 31–47

Contents lists available at ScienceDirect

Journal of Asian Earth Sciences

journal homepage: www.elsevier.com/locate/jseaes

Full length Article

Block-like versus distributed crustal deformation around the northeastern Tibetan plateau

Yanzhao Wang [a], Min Wang [a], Zheng-Kang Shen [b,c,*]

[a] State Key Laboratory of Earthquake Dynamics, Institute of Geology, China Earthquake Administration, Beijing 100029, China
[b] School of Earth and Space Science, Peking University, Beijing 100871, China
[c] Dept. of Earth, Planetary, and Space Sciences, UCLA, Los Angeles, CA 90095-1567, USA

ARTICLE INFO

Article history:
Received 28 August 2016
Received in revised form 22 February 2017
Accepted 27 February 2017
Available online 9 March 2017

Keywords:
GPS
Northeastern Tibetan plateau
Crustal deformation
Deformable-block-motion model
Seismic moment rate

ABSTRACT

It has been debated for decades whether crustal deformation in and around the Tibetan plateau is distributed or block-like. We model crustal deformation in northeastern Tibet using a deformable-block-motion model, in which kinematic parameters of block motion and internal deformation and the associated boundary slip rates are inverted for using GPS velocity data. The F-test is used to screen out station velocity outliers, justify independence of neighboring blocks, and determine the significance of block internal strains through an iteration process. As a result, fifteen blocks are identified, with their boundary faults slipping at rates of 1–10 mm/a. Blocks located east and north of the plateau have large sizes (>10^4 km^2 in area) in general, with little internal deformation. Six blocks within the plateau, in contrast, are smaller in sizes, with internal strain rates on the order of 1–10 nanostrain/a. Five blocks sitting at the northeast borderland of the plateau have small block sizes but no significant internal deformation. Our results show sinistral slip rates of 4.3 ± 1.6 and 4.6 ± 1.8 mm/a across the western and eastern segments of the Haiyuan fault, and 10.8 ± 2.3, 4.6 ± 2.6, and 3.8 ± 2.1 mm/a across the western, central, and eastern segments of the East Kunlun fault, respectively. The southwestern, central, and northeastern segments of the Longmenshan fault slip right-laterally at rates of 1.7 ± 1.1, 1.1 ± 0.8, and 1.1 ± 0.8 mm/a, with shortening rates of 1.1 ± 1.2, 0.4 ± 0.8, and 0.8 ± 1.1 mm/a, respectively. We also develop a scheme to convert geodetic strain rate into seismic moment accumulation rate within blocks and at block boundaries, and estimate the two rates as $\sim 8.40 \times 10^{18}$ and $\sim 2.06 \times 10^{19}$ N·m/a, respectively. In comparison, the corresponding seismic moment release rates are estimated as $\sim 6.06 \times 10^{18}$ and $\sim 2.44 \times 10^{19}$ N·m/a using an contemporary earthquake catalog of 1920–2015. Such results indicate that the seismic moment accumulation and release rates are comparable for the latest 95 years when the earthquake catalog is complete for strong to large events. Both geodetic and seismic estimates suggest that a major portion (~70–80%) of the total seismic moment is accumulated and released at block boundaries, and a minor but still significant portion (~20–30%) is accumulated and released within blocks.

1. Introduction

Unlike most parts of the continental interiors of the world, the Tibetan plateau and its surrounding region have been undergoing intense tectonic deformation, whose evolution has long been the focus of continental dynamics research. The region has also been frequently hit by strong earthquakes, whose locations and mechanisms were usually controlled by faults in and around the plateau. Quantitative research on the distribution of regional crustal deformation and fault slip not only provides valuable data for seismic risk assessment, but also plays an important role in understanding the dynamics underlying the evolution of the Tibetan plateau.

Two alternative end-member models have been proposed on the deformation kinematics and dynamics of the Tibetan plateau. At one extreme, ignoring the plasto-elastic deformation of the crustal medium, the rigid block motion model suggests that the continental lithosphere is composed of a collage of large-scale rigid blocks, whose boundaries are delineated by a limited number of lithospheric strike-slip dominant faults. The eastward extrusion of the plateau is believed to be accommodated by rapid slip along these faults (Tapponnier and Molnar, 1976; Tapponnier et al., 1982, 2001; Peltzer and Tapponnier, 1988; Avouac and Tapponnier, 1993; Peltzer and Saucier, 1996; Replumaz and Tapponnier, 2003). At the opposite extreme, deformation is claimed to be

* Corresponding author at: School of Earth and Space Science, Peking University, Beijing 100871, China.
E-mail address: zhengkangshen@pku.edu.cn (Z.-K. Shen).

http://dx.doi.org/10.1016/j.jseaes.2017.02.040
1367-9120/

widely distributed throughout the continental interior. Plateau uplift is proposed to be the result of bulk crustal shortening and thickening, while contribution of major fault zones to crustal deformation, is discounted or neglected (Vilotte et al., 1982, 1986; England and McKenzie, 1982; Houseman and England, 1986, 1993; England and Molnar, 1997; Flesch et al., 2001). Thatcher (2007) suggested that the two end-member models converge, that although the surface deformation in first-order is block-like, deformation at depth in the ductile part of lithosphere might well be considerably more continuous than it is at the surface. Chen et al. (2004) interpreted an early set of GPS vectors in the Tibetan plateau with a deformation model that the plateau is cut by a few major, rapidly slipping strike-slip fault zones, with broadly distributed strain between those zones.

Wang et al. (2003a) classified the regions in continental China into three categories, demonstrating block-like, intermediate, and distributed deformation respectively. The northeastern Tibetan plateau was considered as of the second category, while stable cratons such as the Ordos terrane was classified as with block-like deformation (Wang et al., 2003a). Such a contrast prompts us to develop a deformable block motion model, which is similar to the one used by Chen et al. (2004), as an effective description of deformation in northeastern Tibetan plateau, and investigate how the deformation is distributed between different tectonic units in the region (Fig. 1). In such a model both deformations in the block and along block boundaries are measured, and their relative weight defines where the reality is situated between the two end member models.

Thanks to the rapid developments of geodetic technology (especially GPS), significant advancements have been made to measure crustal deformation and understand its mechanisms (e.g. Feigl et al., 1993; Reilinger et al., 1997; Bilham et al., 1997; Holt et al., 2000; McCaffrey et al., 2000, 2007; Wang et al., 2001, 2009; Zhang et al., 2004; Wallace et al., 2004; d' Alessio et al., 2005; Meade and Hager, 2005; Loveless and Meade, 2011). When one attempts to use a block motion model to characterize crustal deformation, it is inevitable to address the issue how to qualify a region as a block. As Bird (2003) pointed out, the cumulative number and area of blocks, in a global scale, roughly obey a power law relationship, implying a fractal structure of the crust. Identification of smaller blocks, however, can be challenging, since as the size of a block reduces, it becomes less clear to distinguish deformations within and along the boundaries of the block.

In recent years an approach of cluster analysis has gained momentum to be used for crustal block motion analysis (e.g. Simpson et al., 2012). It has been applied for deformation studies in the Tibetan plateau region (Loveless and Meade, 2011; Zhang and Wei, 2011). We take a different approach to this problem, starting from dividing the studied region into candidate blocks as small as possible, and introducing statistical tests to combine them into larger ones until the kinematic independence between any couple of neighboring blocks exceeds a statistical threshold. The method and result will be compared with the ones using the cluster analysis approach (Loveless and Meade, 2011; Zhang and Wei, 2011). Relative motion rates across block boundaries (i.e. fault slip rates) and mean strain rates within blocks are also estimated, and the results are converted to seismic moment accumulation rates for comparison with earthquake catalog derived seismic moment release rates. The results are further compared with that of a similar study of Wang et al. (2009).

2. GPS data and processing

GPS data used in this study are mainly from the Crustal Motion Observation Network of China (CMONC) project observed in 1999, 2001, 2004, and 2007 in the region of northeastern Tibetan plateau (Wang et al., 2003a; Zhang et al., 2004; Niu et al., 2005; Gan et al., 2007). We also include data from the National Basic Research Project (Wang, 2009), the postseismic survey of the 2001 Mw 7.8 Kokoxili earthquake (Ren and Wang, 2005), and the 1998 Sino-US joint survey in the Altyn Tagh region (Shen et al., 2001).

The GPS data were analyzed using the GAMIT/GLOBK (Herring et al., 2010) and QOCA (http://gipsy.jpl.nasa.gov/qoca/) software (Wang et al., 2003a; Shen et al., 2011). During this process, the GPS data carrier phase data were first processed to obtain loosely constrained daily solutions for station positions and satellite orbits using the GAMIT software. The regional daily solutions were then combined with global solutions produced by the Scripps Orbital and Permanent Array Center (http://sopac.ucsd.edu) using the GLOBK software. In the last step the station positions and velocities were estimated using the QOCA software and referenced to the stable Eurasia plate using a group of IGS sites located in northern Europe and Siberia, and the velocity solution in the studied region is shown in Fig. 2. Most GPS stations spanning the range of 94–106°E, 32–42°N show east-northeastward motion with respect to the Eurasia plate, with their velocities decreasing from ~20 mm/a in southwest to ~5 mm/a in northeast. The velocity field in the studied region also presents a clockwise rotation, which is consistent with previous observations (Wang et al., 2001, 2003a; Zhang et al., 2004; Gan et al., 2007).

3. GPS data inspection and block model parameterization

The results of block models can be very sensitive to the assumed block geometry, and decisions about block boundaries are sometimes made subjectively. We applied a multi-step process to define the block model geometry that is designed to minimize subjective decisions or assumptions. We first select 24 velocity profiles to investigate deformation across faults of potential interest and invert for their slip rates. The region is then divided into 20 initial blocks based on previous geological and geophysical studies and examination of the GPS velocity profiles, with the block boundaries including both faults of known geological significance and faults with significant slip rates inferred from the GPS data. All blocks must have closed boundaries, so these are assumed when the set of active faults is not sufficient by itself to produce a full set of closed blocks. Adjacent blocks are then combined if they are not statistically independent according to the F-test, resulting in the final block model geometry. The detailed procedure is described below.

3.1. Velocity profiles

In order to define the block geometry, we first investigate differential motions across faults determined from previous geological and geophysical studies (e.g. Deng et al., 2003; Guo et al., 2000). In addition, localized velocity gradient zones are identified as block boundaries in the initial model. GPS velocity profiles are used for close examination and fault slip rates are estimated accordingly. To better visualize the differential motion across a fault, we choose one side of the fault as reference where the station velocities show more consistent motion than the other side of the fault. A best-fit Euler vector is determined by using all the GPS observations within the reference block, and the corresponding velocity field with respect to the block is obtained by removing the rigid body rotation component from all the GPS stations. Velocities of involved GPS stations are decomposed into strike-parallel and strike-normal components respectively.

For an infinitely-long strike-slip fault locked above and creeping below the locking depth, the associated surface velocity field along

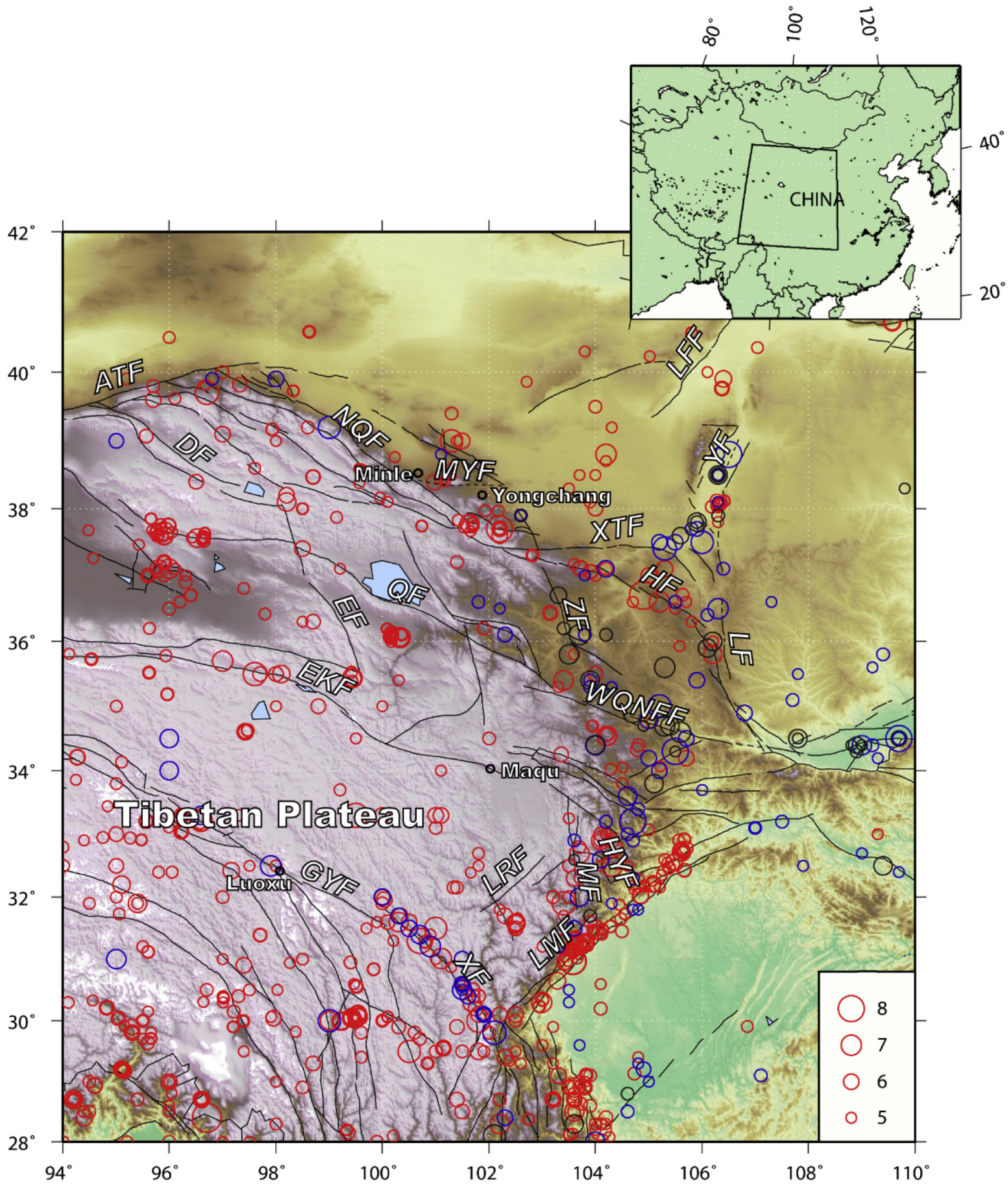

Fig. 1. Topography and active faults in the studied area. Abbreviations are: ATF, the Altyn Tagh fault; NQF, the Northern Qilian fault; MYF, the Minle-Yongchang fault; HF, the Haiyuan fault; XTF, the Xiangshan-Tianjingshan fault; DF, the Danghenanshan fault; QF, the Qinghainanshan fault; EKF, the East Kunlun fault; GYF, the Ganzi-Yushu fault; XF, the Xianshuihe fault; ZF, the Zhuanglanghe fault; WQNFF, the West Qinling Northern Frontal fault; YF, the Yinchuan fault; LF, the Liupanshan fault; EF, the Elashan fault; LRF, the Longriba fault; MF, the Minjiang fault; HYF, the Huya fault; LMF, the Longmenshan fault; LFF, the Langshan Frontal fault. Red, blue, and black circles denote earthquakes of M > 5 occurred during the periods of 1920–2015, 1550–1920, and 780 BCE–1550, respectively (Gu, 1983; http://www.csndmc.ac.cn/newweb/data.htm (For interpretation of the references to color in this figure legend, the reader is referred to the web version of this article.)

the fault-normal direction can be approximated by a function V(x) = $\frac{v}{\pi}\arctan\frac{x}{D}$, where v is the fault creep rate at depth, D the locking depth, and x the distance from the fault (Savage and Burford, 1973). We employ the same functional form to model crustal deformation field across a dip-slip fault, although it is only an approximation of a more complex deformation field; in this step, the goal is simply to identify the locations of the block boundaries and obtain rough estimates of fault slip rates. Some of the far-field data points affected by slip on other faults are omitted and the remaining data are used to determine deformation across the fault segments under investigation. The along-strike and fault-normal components of the slip rates are estimated by fitting the arctangent function to the fault-parallel and normal components of the station velocities. Based on the range of earthquake depths in the studied region (Wang et al., 2000; Yang et al., 2003, 2004; Sun et al., 2006; Li and Xu, 2010; Xin et al., 2010; Liu et al., 2011a,b; Wan et al., 2012), we fix the fault locking depth D at 20 km. (We also estimated slip rates with locking depths of 10 and 15 km, and the results do not differ much from that of 20 km.) At the same time, uncertainties of slip rates are also obtained through propagating formal uncertainties of GPS velocities.

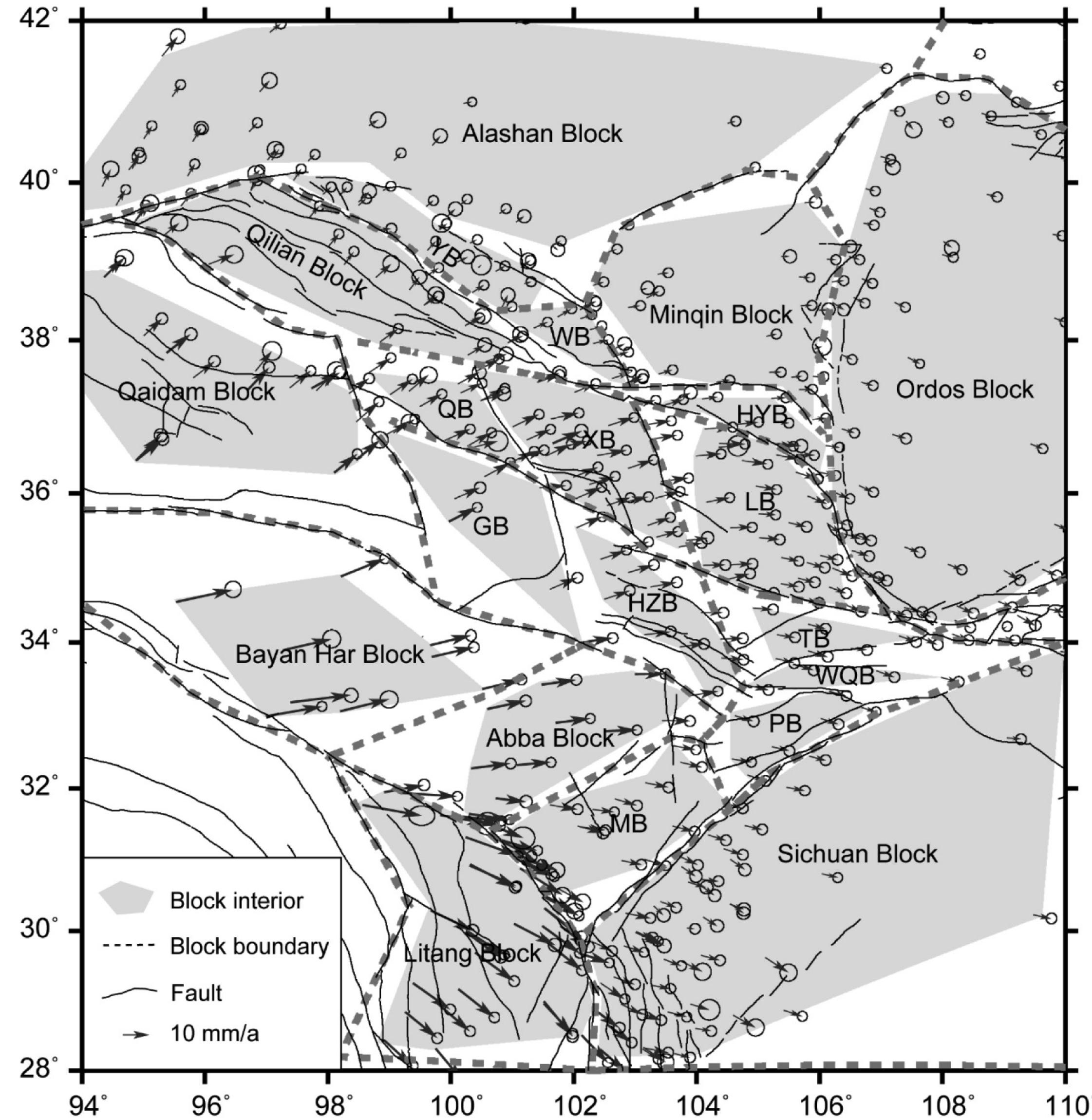

Fig. 2. GPS horizontal velocity field of the northeastern Tibetan plateau and the micro-block model. Gray areas represent the interior of the initial blocks, dashed lines are the final block boundaries, and arrows are the GPS velocities with respect to the Eurasia plate, with the error ellipses representing 70% confidence. Abbreviations are: YB, Yumushan block; WB, Wuwei block; HYB, Haiyuan block; QB, Qinghai block; XB, Xining block; WQB, West Qinling block; LB, Lanzhou block; GB, Guinan block; HZB, Hezuo block; TB, Tianshui block; PB, Pingwu block; MB, Maerkang block.

As shown in Fig. 3, involved GPS stations for each concerned fault or velocity gradient zone are encompassed by gray frames, and the corresponding velocity profile across fault that demonstrates the differential motion is shown in Fig. 4. Most faults we outlined are justified to have significant slip at more than 90% confidence by the F test (Table 1), with their slip rates ranging from 0.1 to 5.1 mm/a for the convergence/extension component, and from 0.1 to 16.1 mm/a for the strike-slip component (Table 1 and Fig. S1). Most of the WNW-trending faults primarily slip left laterally, and most of the NNW-trending and NE-trending faults are dominated by dextral slip, respectively. Among the velocity profiles, those with good coverage of near-field stations and significant cross-fault differential motion play an important role in determining the locations of block boundaries, such as those across the Minle-Yongchang, Haiyuan, Xiangshan-Tianjingshan, Ganzi-Yushu, Xianshuihe, Yinchuan, and Liupanshan faults. While others are less helpful and we primarily rely on the information from previous geological and geophysical studies to locate the remaining block boundaries.

3.2. Initial block geometry

Based on the significant velocity gradients shown in the GPS velocity field, we modify the block model of Guo et al. (2000) and divide the studied area into 20 blocks initially. The boundaries of the Qilian block are determined relying on the profiles A, B, C, D and N. Profiles G, R, J, and K are helpful for separating the Guinan and Hezuo blocks from the other blocks. The Lanzhou block is delineated according to the profiles F, H, P, and Q. The profiles I, J, and X are used for tracing the boundaries the Bayan Har block. The boundaries of the Litang block are determined according to the profiles L and M. The profiles E and O contribute to investigate the extent of the Alashan block. The Sichuan block is separated from the other blocks according to the profiles S, T, and U. The profiles V and W help for delineating the Maerkang block.

Although the velocity field is mostly continuous and coherent (Fig. 2), we identify and remove a few possible outliers in the dataset. The station velocity outliers are detected and removed in two steps. We first delete obvious outliers which are clearly at odds

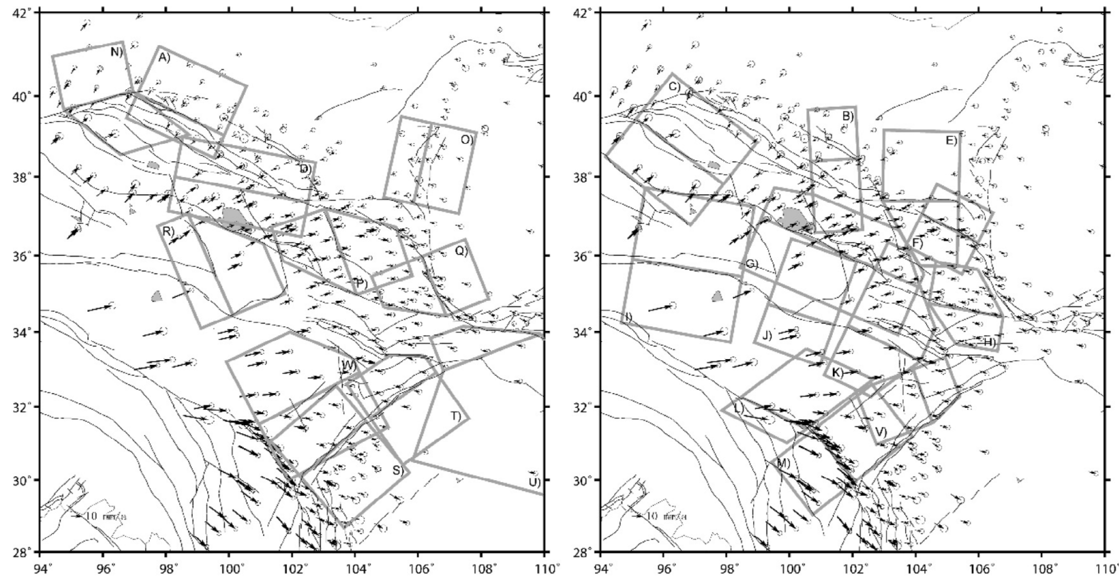

Fig. 3. GPS velocity field with respect to Eurasia plate. The gray polygonal frames encompassing fault segments mark the regions within which stations are depicted for slip rate estimation.

with the neighboring sites by visual inspection. We then use the F-test to screen out station velocity outliers within each block and justify the block model through an iteration process, each time removing a site with the largest post-fit residual, or modifying a block boundary to allow the site to shift into another block. During this process, the blocks are assumed to be rigid for simplicity. For a given block, velocities of all the stations within the block are inverted for the Euler rotation vector using the least squares regression, with the corresponding post-fit residual χ^2_{n} evaluated at the same time, where n is the number of sites in the block. The site with the largest post-fit residual is then removed and the remaining station velocities are used to estimate the Euler vector and the post-fit residual χ^2_{n-1} again. The F value is defined as:

$$F = F(\chi^2_{\mathrm{n}},\ 2n-3;\ \chi^2_{n-1},\ 2n-5) = \frac{\chi^2_n/(2n-3)}{\chi^2_{n-1}/(2n-5)}, \tag{1}$$

and the probability P(F) is evaluated. If the F-test exceeds 95% confidence, we will remove the site or modify the block boundary. The procedure is ceased when F-test yields <95% confidence, and moves to the next block. This procedure is similar to the one used by Wang et al. (2003a) for outlier detection.

3.3. Final block geometry

A procedure similar to the one described above is implemented for evaluating independence of neighboring blocks using the F-test. Again assumption of rigid block motion is taken as it is considered to be the first-order description of crustal deformation. The F-test result of block independence is listed in Table S1. Taking into account of the block geometry and kinematic compatibility, adjacent blocks whose independence is lower than 70% confidence are merged together. The Hezuo, Xining, Yumushan, Wuwei, and Pingwu blocks are merged into the Guinan, Qinghai, Alashan, Qilian, and West Qinling blocks, respectively. Since independence between the Tianshui and the merged Pingwu and West Qinling blocks is at only 54.0% confidence, they are furthermore merged together. After combination, all of the neighboring blocks are independent of each other at more than 70% confidence (Table S2, Fig. 2).

Since the GPS station coverage is not dense enough everywhere in the studied region for delineating reliable block boundaries, we show regions identified as block interiors in gray, and leave the regions containing possible block boundaries as blank in Fig. 2. We then identify possible block boundaries based on geologic and geophysical data (Deng et al., 2003; Guo et al., 2000). The boundaries between the Alashan and Qilian blocks are defined as the Altyn Tagh, Northern Qilian, and Minle-Yongchang faults. The Langshan Frontal, Wuwei-Tianzhu, Xiangshan-Tianjingshan, and Yinchuan faults are delineated as the boundaries between the Minqin block and Alashan, Qilian, Haiyuan, and Ordos blocks, respectively. We choose the Danghenanshan and western segment of the Haiyuan faults as the boundaries between the Qilian block and the Qaidam and Qinghai blocks, respectively. The Elashan fault is set as the boundary between the Qaidam block and the Qinghai and Guinan blocks. The boundaries between the Lanzhou block and the Haiyuan, Qinghai, West Qinling, and Ordos blocks are defined as the eastern Haiyuan, Zhuanglanghe, West Qinling Northern Frontal (WQNF), and Liupanshan faults, respectively. The Qinghainanshan fault is determined as the boundary between the Qinghai and Guinan blocks. The East Kunlun fault separates the Qaidam and Guinan blocks from the Bayan Har and Abba blocks. The Ganzi-Yushu-Xianshuihe fault delineates the boundaries between the Litang block and the Abba, Maerkang, and Sichuan blocks. The boundaries between the Maerkang block and the Abba, West Qinling, and Sichuan blocks are defined as the Longriba, Huya, and western Longmenshan faults. We choose the central and eastern segments of the Longmenshan fault as the boundary between the Sichuan and West Qinling blocks. These block boundaries are to a certain degree similar to the ones adopted in the model of Loveless and Meade (2011) and have less in common with those in Thatcher (2007) (as shown in Fig. S2), and a detailed comparison between the three realizations will be made in the Discussion section.

4. Deformabale block motion model

In the deformable block motion model (DBM), we assume that the surface velocity field is the result of boundary slips associated with relative block motion and possible internal deformation.

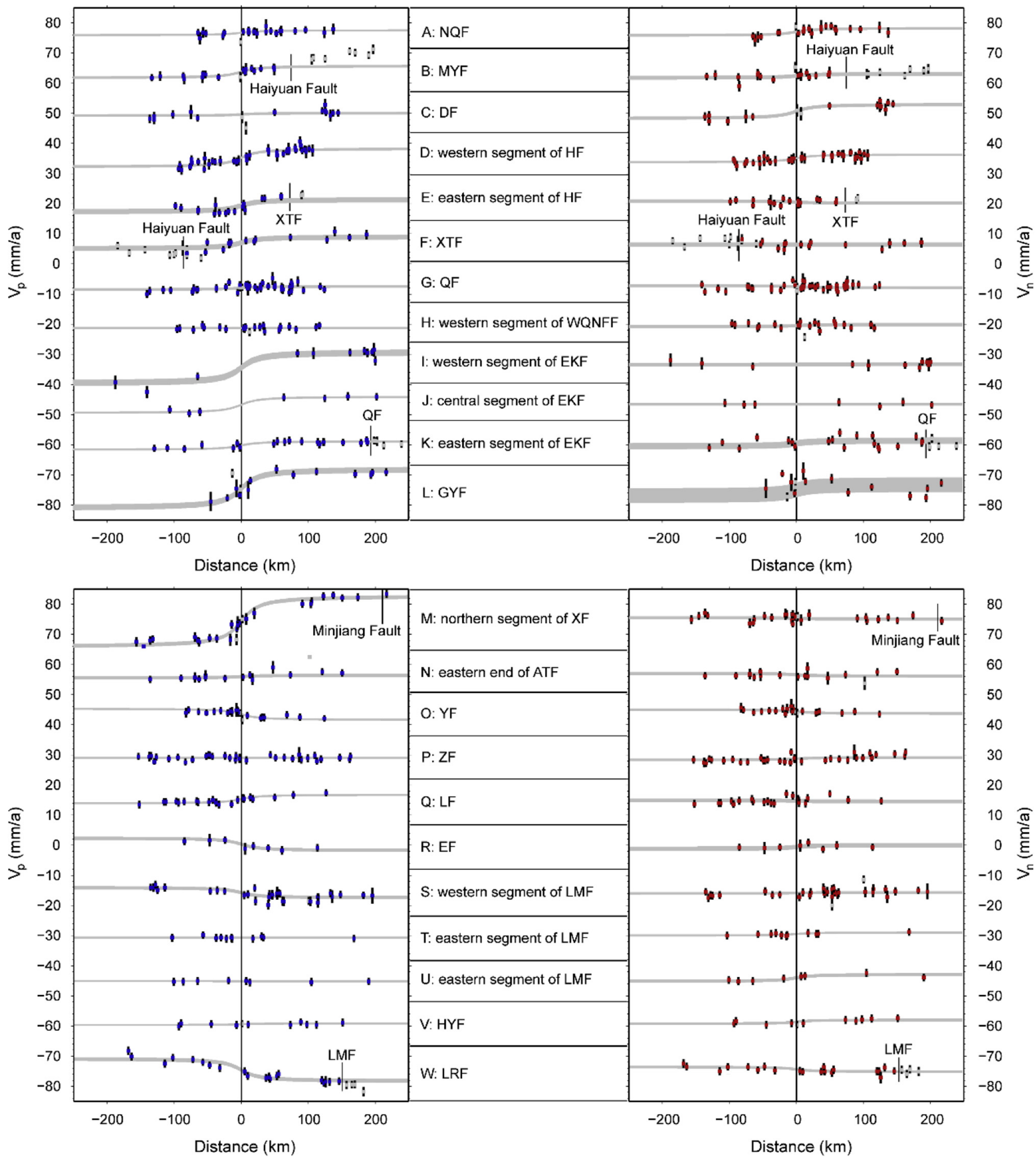

Fig. 4. GPS velocity profiles across fault segments. Left and right panels are fault-parallel (sinistral positive) and fault-normal (shortening positive) components respectively. Blue and red squares represent data used for calculating the slip rates, while the gray ones represent those omitted from calculation due to poor data quality, near field complication, and/or contamination by slips of other faults. Short vertical bars are the uncertainties of station velocity components, and a few vertical bars show the locations of other faults w.r.t. the ones whose slip rates are being evaluated. Widths of the gray curves show 1-σ uncertainties of the model predicted inter-seismic deformation across faults. (For interpretation of the references to color in this figure legend, the reader is referred to the web version of this article.)

Block boundaries are delineated by active faults. All the block boundaries are assumed to be vertical and composed of upper brittle and lower creeping zones. The brittle zone represents the seismogenic portion of faults that is locked during the interseismic period, and the amount of dislocation across the creeping zone is determined by the relative motion between the neighboring blocks less their internal deformation. In the kinematic framework, the crustal deformation associated with relative block motion during the interseismic period is understood as the superposition of a rigid block motion with creeping fault at the boundaries and virtual slip at opposite direction on the seismogenic zone, which is generally called "backslip" analogous to that at subduction zone (Savage, 1983). Therefore, the station velocity at an arbitrary spot ($\vec{V^i}$) represents the sum of $\vec{V_b^i}$ and $\vec{V_f^i}$, where $\vec{V_b^i}$ is associated with

Table 1
Results of fault slip rate estimates.

Num	Faults	Significance (%)	Normal component (mm/a, + extensional)		Strike-slip component (mm/a, + dextral)		Geological estimates (mm/a, + extensional/dextral)	Geodetic estimates (mm/a, + extensional/dextral)
			DBM	VPP	DBM	VPP		
1	NQF	**100.0**	*−1.5 ± 1.0*	*−3.1 ± 0.4*	−1.1 ± 1.0	−1.3 ± 0.3	∼2 (Institute of Geology, State Bureau of Seismology, 1993)	
2	MYF	**100.0**	−0.7 ± 0.9	−1.0 ± 0.6	−3.1 ± 0.7	−3.5 ± 0.4		
3	DF	**100.0**	*−0.4 ± 1.9*	*−5.1 ± 0.5*	−2.8 ± 1.7	−2.0 ± 0.4		
4	HF							
	Western segment	**100.0**	*0.3 ± 2.0*	*−2.7 ± 0.3*	−4.3 ± 1.6	−5.8 ± 0.4	−10 to −5 (Burchfiel et al., 1991); −4.5 ± 1.0 (Li et al., 2009); *−11 ± 4* (Gaudemer et al., 1995)	−5 (Wang et al., 2003a); −5 ± 1 (Zhang et al., 2004); −8 to −4.2 (Cavalié et al., 2008); −4.6 ± 0.1 (Loveless and Meade, 2011); *−12 ± 4* (Lasserre et al., 1999, 2002)
	Eastern segment	**100.0**	−2.6 ± 2.5	−0.5 ± 0.5	−4.6 ± 1.8	−5.4 ± 0.8		−5 (Wang et al., 2003a)
5	XTF	**100.0**	0.2 ± 2.7	0.4 ± 0.7	−3.1 ± 2.3	−4.3 ± 0.8	∼−3 (Li, 2005)	
6	QF	**97.3**	−1.0 ± 1.5	−0.8 ± 0.4	−2.4 ± 1.2	−1.0 ± 0.4		
7	WQNFF	27.3	−0.3 ± 1.1	0.1 ± 0.5	−1.3 ± 1.0	−0.2 ± 0.3	−2.3 ± 0.2[a] (Li et al., 2007)	*−7.0 ± 0.4* and *−7.5 ± 0.4*[a] (Loveless and Meade, 2011)
8	EKF							
	Western segment	**100.0**	1.7 ± 2.5	−0.2 ± 0.6	−10.8 ± 2.3	−10.6 ± 1.0	−11 ± 2 (Van der Woerd et al., 1998, 2000, 2002); −12 to −8 (Kirby, 2007); −10.0 ± 1.5 (Li et al., 2005);	∼−13.7 (Gan et al., 2007); −14.9 ± 1.1 (Wang et al., 2009); −9.3 to 10.8 (Loveless and Meade, 2011)
	Central segment	**100.0**	−2.5 ± 2.9	0.1 ± 0.4	−4.6 ± 2.6	−5.5 ± 0.3	−6 to −4 at 101.4°E (Kirby et al., 2007); −2.0 ± 0.4 at 101.8°E (Kirby et al., 2007); ∼*−10* at *99*°E and *−12.5 ± 2.5* at *100.5*°E (Van der Woerd et al., 2000, 2002)	−5 to −3 (Kirby et al., 2007); −5.0 (Loveless and Meade, 2011); ∼*−8.7* (Gan et al., 2007)
	Eastern segment	**96.7**	0.7 ± 2.3	−0.8 ± 1.0	−3.8 ± 2.1	−2.2 ± 0.3	<*1* mm/a at *103.1*°E (Kirby et al., 2007)	−3.3 ± 1.5 (Wang et al., 2009); −2.0 (Loveless and Meade, 2011)
9	SE segment of GYF	**100.0**	6.8 ± 2.2	4.3 ± 2.4	−10.4 ± 2.1	−12.3 ± 0.9	−12 ± 2 (Wen et al., 2003); −14 ± 3 (Xu et al., 2003a);	−13.0 to −3.1 (Wang et al., 2008); −9.6 ± 1.3 (Wang et al., 2009); −14.6 to −10.2 (Loveless and Meade, 2011); −6.6 ± 1.5 (Wang et al., 2013)
10	XF	**100.0**	−1.9 ± 1.4	0.4 ± 0.5	−14.3 ± 1.6	−16.1 ± 0.6	−15 ± 5 (Allen et al., 1991); −14 ± 2 (Xu et al., 2003a)	*−11* to *−10* (Shen et al., 2005); ∼−14.4 (Gan et al., 2007); −15.7 to −11.2 (Wang et al., 2008); −16.5 ± 0.8 (Wang et al., 2009); *−9.7 ± 0.7* (Wang et al., 2013); *−11.6* to *−9.6* (Loveless and Meade, 2011)
11	Eastern end of ATF	**98.3**	−1.1 ± 1.6	−0.6 ± 0.5	−1.3 ± 1.4	−1.7 ± 0.5	*−5* to *−4* (Wang et al., 2003b); *−11* to *−2* (Xu et al., 2003b); *−13* to *−9* (Mériaux et al., 2005)	−4.3 to −1.6∼ (Gan et al., 2007); −1.3 ± 0.4 (Wang et al., 2009); *−5.1 ± 0.6* (Loveless and Meade, 2011)
12	YF	**100.0**	0.4 ± 0.9	0.9 ± 0.4	2.8 ± 1.0	2.6 ± 0.3		
13	ZF	**99.9**	−1.4 ± 1.3	−1.5 ± 0.4	−0.4 ± 1.3	0.1±0.3		0.6 ± 1.5 and −0.5 ± 1.5[a] (Zhou et al., 2005)
14	LF	**100.0**	−1.0 ± 1.1	−1.3 ± 0.6	−1.6 ± 1.1	−2.7 ± 0.3		−2.7 to −0.5 (Gan et al., 2007)
15	EF							
	Northern segment	**99.5**	−0.3 ± 2.0	−0.3 ± 0.7	1.0 ± 2.1	3.3 ± 0.5		1.0 ± 0.8 (Loveless and Meade, 2011)
	Southern segment		1.1 ± 2.7		3.5 ± 1.7		4.1 ± 0.9 (Yuan et al., 2004)	4.2 ± 0.4 (Loveless and Meade, 2011)
16	LMF							
	Western segment	**100.0**	−1.1 ± 1.2	−1.2 ± 0.4	1.7 ± 1.1	3.1 ± 0.5		1.7 ± 0.8 and 1.2 ± 1.0[a] (Wang et al., 2009); *2.8–3.5* and *3.2–4.2*[a] (Loveless and Meade, 2011)
	Central segment	85.5	−0.4 ± 0.8	−0.8 ± 0.3	1.1 ± 0.8	0.2 ± 0.3		1.4 ± 1.1 and 3.3 ± 1.3[a] (Wang et al., 2009); *2.8–3.5* and *3.2–4.2*[a] (Loveless and Meade, 2011)
	Eastern segment	**99.5**	−0.8 ± 1.1	−1.9 ± 0.5	1.1 ± 0.8	−0.1 ± 0.3		
17	HYF	**98.0**	−1.0 ± 1.3	−1.4 ± 0.4	−1.1 ± 1.9	−0.4 ± 0.3		
18	LRF	**100.0**	−0.6 ± 1.5	1.2 ± 0.4	*4.9 ± 1.5*	*7.6 ± 0.6*		4–6 (Shen et al., 2005); ∼*2* (Loveless and Meade, 2011)

[a] Normal component. Significances beyond 95% are bold. Inconsistent results are shown as italics.

rigid block motions and possible internal deformation, and $\vec{V}_f^i$ with back-slips on block boundaries above the fault locking depth, respectively.

Since the sizes of most blocks in the studied region are on the order of $1° \times 1°$, biases introduced by neglecting the effects of earth curvature in the deformation modeling are much smaller than the errors of GPS velocity field. We therefore use a simple Cartesian coordinate system in the modeling work. The horizontal components of $\vec{V}_b^i$ at any given spot within a homogeneously deformed block are then written in the following form (Shen et al., 1996):

$$\begin{pmatrix} V_x^i \\ V_y^i \end{pmatrix} = \begin{pmatrix} 1 & 0 & \Delta x_i & \Delta y_i & 0 & \Delta y_i \\ 0 & 1 & 0 & \Delta x_i & \Delta y_i & -\Delta x_i \end{pmatrix} \begin{pmatrix} U_x \\ U_y \\ \dot{\varepsilon}_{xx} \\ \dot{\varepsilon}_{xy} \\ \dot{\varepsilon}_{yy} \\ \dot{\omega} \end{pmatrix} + \begin{pmatrix} e_x^i \\ e_y^i \end{pmatrix} \tag{2}$$

where V_x^i and V_y^i are the observed east and north velocity components of the i-th station at a location $\vec{r}_i$. All the variables on the right-hand side of the equation are to be evaluated at the geometric center of the station network within the block ($\vec{R}$). Δx_i and Δy_i are the vector components of $\Delta \vec{R}_i = \vec{r}_i - \vec{R}$. U_x and U_y are the translation velocity components of the block. $\dot{\varepsilon}_{xx}$ and $\dot{\varepsilon}_{yy}$ are the normal strain rates, $\dot{\varepsilon}_{xy}$ is the shear strain rate, and $\dot{\omega}$ is the rotation rate. e_x^i and e_y^i are the errors of the corresponding velocity components at the i-th station. When $\dot{\varepsilon}_{xx} = \dot{\varepsilon}_{yy} = \dot{\varepsilon}_{xy} = 0$, the equation is reduced to represent a rigid block motion model, and the parameters U_x, U_y, and $\dot{\omega}$ are related to the block angular velocity in the spherical case.

In general, a model with more parameters will result in smaller post-fit residuals, which however does not necessarily justify that to be a better model. Additional parameters are justified only when their reduction of the post-fit residual χ^2 is statistically significant. Therefore, parameters representing homogeneous strain rate within a block, i.e. $\dot{\varepsilon}_{xx}$, $\dot{\varepsilon}_{yy}$, and $\dot{\varepsilon}_{xy}$ in the above equation, are not necessary unless the reduction of the post-fit residual χ^2 can pass the F-test to verify its significance in improving the model.

To account for the fault locking effect at block boundaries to station velocities, we divide block boundaries into segments of tens of kilometers in length and deduce their slip rates from relative block motions. The fault locking effect is realized through a back-slip model, with the Green's functions computed using the Okada (1992) dislocation code linking fault slip rates to GPS station velocities. A uniform locking depth of 20 km is assumed for all the fault segments as adopted in fault slip estimation by means of velocity profiles. This value is different from the locking depth of 16 km found by Loveless and Meade (2011) based on velocity residual statistics, but still within the common error margins.

We first choose the Alashan block as the local reference frame (Fig. 2), whose Euler vector with respect to Eurasia plate is estimated as (75.388°W, 35.047°E, 5.81 nanorad/a) using velocities of stations within the block, and obtain the velocity field with respect to the Alashan block by removing its rigid body rotation from the velocity field. This process is important because the data uncertainties are much smaller referenced to a local reference than to the stable Eurasia plate by reducing positive correlations between nearby stations due to the intrinsic nature of covariances in GPS velocity solutions.

Constrained by these station velocities, we invert for parameters of all other blocks simultaneously. Through an iteration process, we justify the significance of internal deformation within each block one by one in the increasing order of their overall uncertainties of translation and rotation rates in the initial rigid block model. For each block, we add 3 strain rate parameters in the inversion during the iteration, and use the F-test to compare the post-fit residual χ^2s obtained in the current and previous iteration steps. Once the internal deformation significance of one block exceeds 99% confidence, the block will always be modeled with internal deformation in the following iteration steps. The iteration is stopped when improvement in model parameter estimation becomes trivial. Following this analysis, seven blocks are determined to have demonstrated significant internal deformation, and eight others are deemed as rigid (Table 2, Figs. 5 and 6).

As mentioned above, we choose the Alashan block as the local reference frame, which demonstrates no internal deformation. Our inversion results also show little or no (<3 nanostrain/a) internal deformation for the Minqin, Ordos, and Sichuan blocks, implying that these blocks are relatively stable in the studied region. This finding is consistent with previous study results suggesting cold/strong cratonic structure of the Ordos and Sichuan blocks, characterized by high seismic velocity of upper mantle and flattened Moho interface (Wang et al., 2003b; Huang et al., 2003; Lebedev and Nolet, 2003; Lai et al., 2004; Guo et al., 2004; Chen et al., 2005; Zhao et al., 2005; Li et al., 2006, 2008; Wu et al., 2006; Ma et al., 2007).

The Qilian and Haiyuan blocks form a WNW-ESE trending narrow stripe, with relatively high left-lateral slip and moderate shortening rates across their northern and southern boundaries. The principal compressional strain rate and the maximum shear strain rate within the Qilian block are 23.2 ± 7.0 nanostrain/a oriented NNE-SSW and 14.0 ± 3.6 nanostrain/a oriented NNW-SSE, respectively. Their narrow stripe geometries make it difficult to distinguish between fault locking effects and internal deformation within the block. Our results reveal a regional deformation pattern of NNE-trending shortening and WNW-trending sinistral shear, which agrees with the results of previous geodetic studies obtained by Wang et al. (2002) and Zhang et al. (2002). Research on neotectonics and active faults also shows strong deformation throughout the region of the Qilian range (Institute of Geology, State Bureau of Seismology, 1993).

In the center of the studied region, the magnitudes of the translation rates of the Qaidam, Qinghai, Lanzhou, Guinan, West Qinling, Bayan Har, Abba, and Maerkang blocks decrease from southwest to northeast, and their translation directions turn clockwise from northwest to southeast. The Qaidam, Bayan Har, Qilian, West Qinling, and Maerkang blocks rotate counter-clockwise, while the Qinghai, Lanzhou, Haiyuan, Guinan, and Aba blocks rotate clockwise, respectively (Fig. 5).

Our results show a ~10 mm/a southeastward motion of the Litang block with respect to the Maerkang block, with a clockwise rotation and an extensional strain rate of 13.7 ± 2.2 nanostrain/a trending NNE-SSW within the block. We infer that its motion is associated with the eastward extrusion of the Tibetan plateau and the gravitational push due to sharp elevation gradient from northwest to southeast in the region.

5. Slip rates along major faults

We estimate slip rates along major faults in the studied region through GPS velocity projection profile (VPP) and inversion results of the DBM, respectively (Table 1). Since the block boundaries are separated into smaller fractions in the DBM, we determine the slip rate across each fault/fault-segment as the averaged slip rates across the fractions weighted by their lengths. The results show that most faults in the studied region fall into three groups, each sharing similar strike and mostly the same deformation style.

Table 2
Inversion results of DBM.

Blocks	Num of stations	Coordinate of the reference point (°)		Translation rate		Rotation rate[a] (nanorad/a)	Internal deformation significance (%)	Maximum normal strain (10^{-9}/a)	Minimum normal strain[b] (10^{-9}/a)	Direction of the minimum[b] strain(°)	Maximum shear strain (10^{-9}/a)
		Longitude	Latitude	Magnitude (mm/a)	Direction (°)						
Alashan	49	100.38	41.06	/	/	/	68.6	0.9 ± 1.5	−1.5 ± 1.0	63.7 ± 22.8	1.2 ± 0.9
Minqin	25	104.47	38.62	2.2 ± 0.4	61.0 ± 10.2	−2.89 ± 0.07	4.34	−0.1 ± 2.7	−2.2 ± 4.1	29.3 ± 62.5	1.0 ± 2.5
Ordos	54	108.44	37.80	2.8 ± 0.2	84.1 ± 5.8	−9.07 ± 0.02	**99.9**	2.7 ± 0.7	0.8 ± 1.0	57.8 ± 18.8	0.9 ± 0.6
Qilian	35	98.66	38.70	3.3 ± 0.5	55.8 ± 9.6	−4.63 ± 0.12	**99.9**	4.8 ± 1.7	−23.2 ± 7.0	26.6 ± 7.6	14.0 ± 3.6
Haiyuan	10	104.84	36.98	5.0 ± 0.6	94.8 ± 9.5	4.69 ± 0.30	78.2	23.8 ± 11.8	−10.6 ± 11.5	66.6 ± 13.0	17.2 ± 9.23
Qaidam	18	95.64	37.16	8.4 ± 0.4	64.4 ± 3.1	−6.41 ± 0.07	**99.4**	1.6 ± 1.5	−12.0 ± 4.0	26.6 ± 8.8	6.8 ± 2.1
Qinghai	39	101.32	36.78	9.0 ± 0.3	77.5 ± 3.4	6.08 ± 0.10	**100.0**	11.3 ± 3.5	−5.5 ± 5.6	171.0 ± 11.1	8.4 ± 3.3
Lanzhou	29	104.94	35.73	8.4 ± 0.3	93.2 ± 2.7	17.17 ± 0.09	66.6	2.8 ± 3.8	−9.0 ± 5.2	8.0 ± 14.3	5.9 ± 3.4
Guinan	18	101.75	35.02	11.1 ± 0.4	79.0 ± 3.0	1.87 ± 0.08	94.6	5.7 ± 2.7	−6.5 ± 7.6	48.1 ± 19.1	6.1 ± 3.8
Bayan Har	7	97.16	34.32	20.9 ± 0.6	86.8 ± 1.9	−7.94 ± 0.13	**100.0**	6.6 ± 8.3	−14.8 ± 3.5	86.6 ± 11.2	10.7 ± 4.4
Abba	11	101.36	32.70	16.2 ± 0.4	90.9 ± 1.9	2.65 ± 0.14	**100.0**	12.4 ± 7.0	−13.7 ± 3.6	80.2 ± 9.6	13.0 ± 3.8
Maerkang	19	102.69	31.42	11.1 ± 0.4	105.8 ± 2.8	−4.32 ± 0.12	68.7	6.7 ± 4.3	−6.6 ± 6.5	134.0 ± 16.32	6.6 ± 3.8
West Qinling	19	106.10	33.54	8.2 ± 0.3	96.1 ± 2.7	−5.21 ± 0.07	80.6	6.0 ± 3.4	−4.5 ± 3.2	108.4 ± 13.2	5.2 ± 2.4
Litang	27	100.29	29.72	23.4 ± 0.3	124.5 ± 0.8	16.03 ± 0.05	**100.0**	13.7 ± 2.2	−5.8 ± 2.4	121.3 ± 4.8	9.7 ± 1.6
Sichuan	45	107.66	30.42	9.4 ± 0.2	89.7 ± 2.2	−7.52 ± 0.02	45.8	2.0 ± 1.6	−0.6 ± 0.8	50.0 ± 19.0	1.3 ± 0.9

[a] Rotation is measured from north, clockwise positive.
[b] Normal strain rates are measured extensional positive. Internal deformation significance beyond 99% are bold.

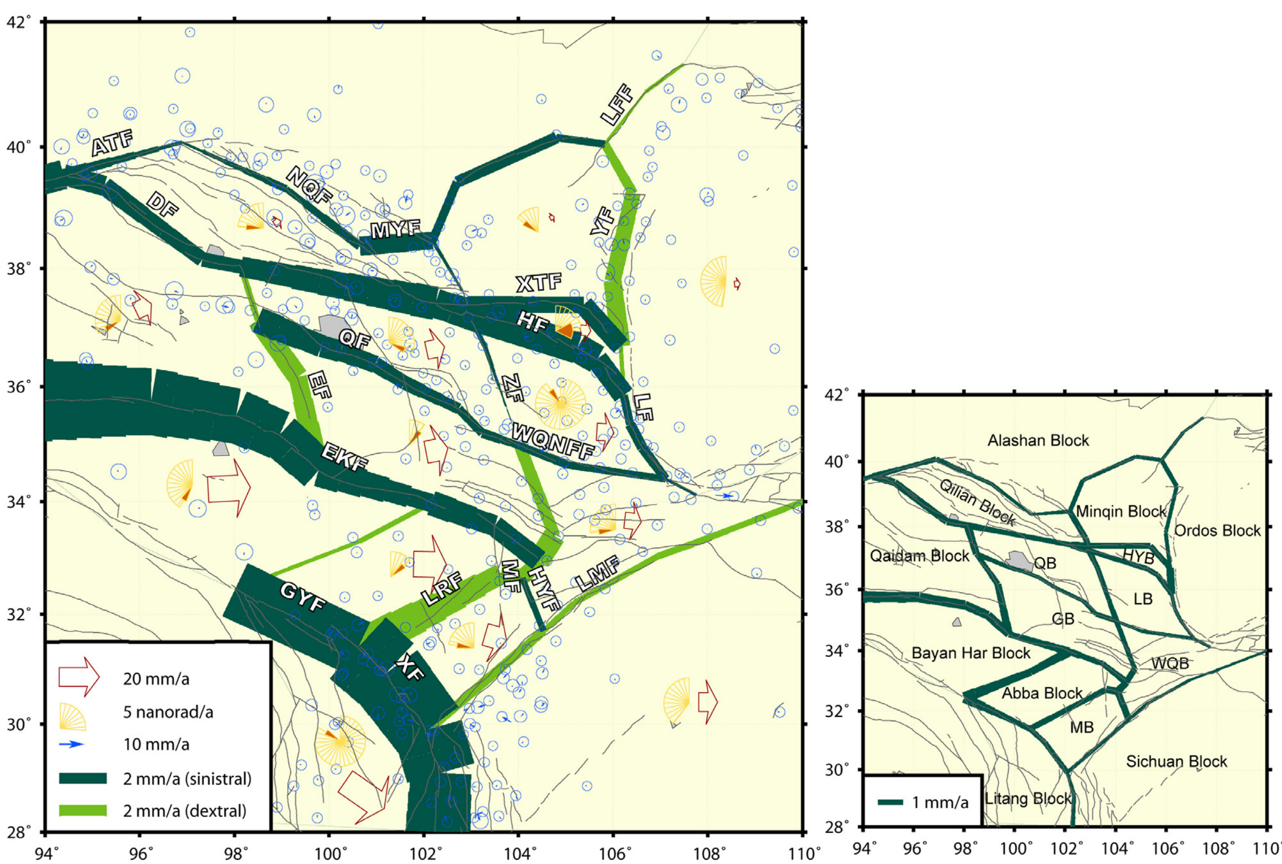

Fig. 5. Inversion results of DBM. The left panel shows translation and rotation rates of the blocks and strike-slip rates across faults. The fan-shaped symbols denote block rotation rates referenced to zero azimuth, with their 5-σ uncertainties marked by fans with smaller radii. Hollow arrows are the translation rate vectors of blocks. Values of the translation and rotation rates are listed in Table 2. The right panel shows the uncertainties of fault shear slip rates.

The WNW trending faults include the Northern Qilian, Minle-Yongchang, Danghenanshan, Xiangshan-Tianjingshan, Haiyuan, Qinghainanshan, WQNF, and East Kunlun faults. These faults and the Ganzi-Yushu-Xianshuihe fault are characterized by left-lateral slip, and most of them have thrust components. The NNW-NS trending faults such as the Elashan, Yinchuan, and Huya faults, slip right-laterally, with their slip rates much lower than those of WNW-trending faults. The Altyn Tagh, Langshan Frontal, Longmenshan, and Longriba faults belong to the ENE to NNE trending group. Detailed results are shown in Figs. S1, 5 and 6, and comparisons with estimations from previous studies are listed in Table 1.

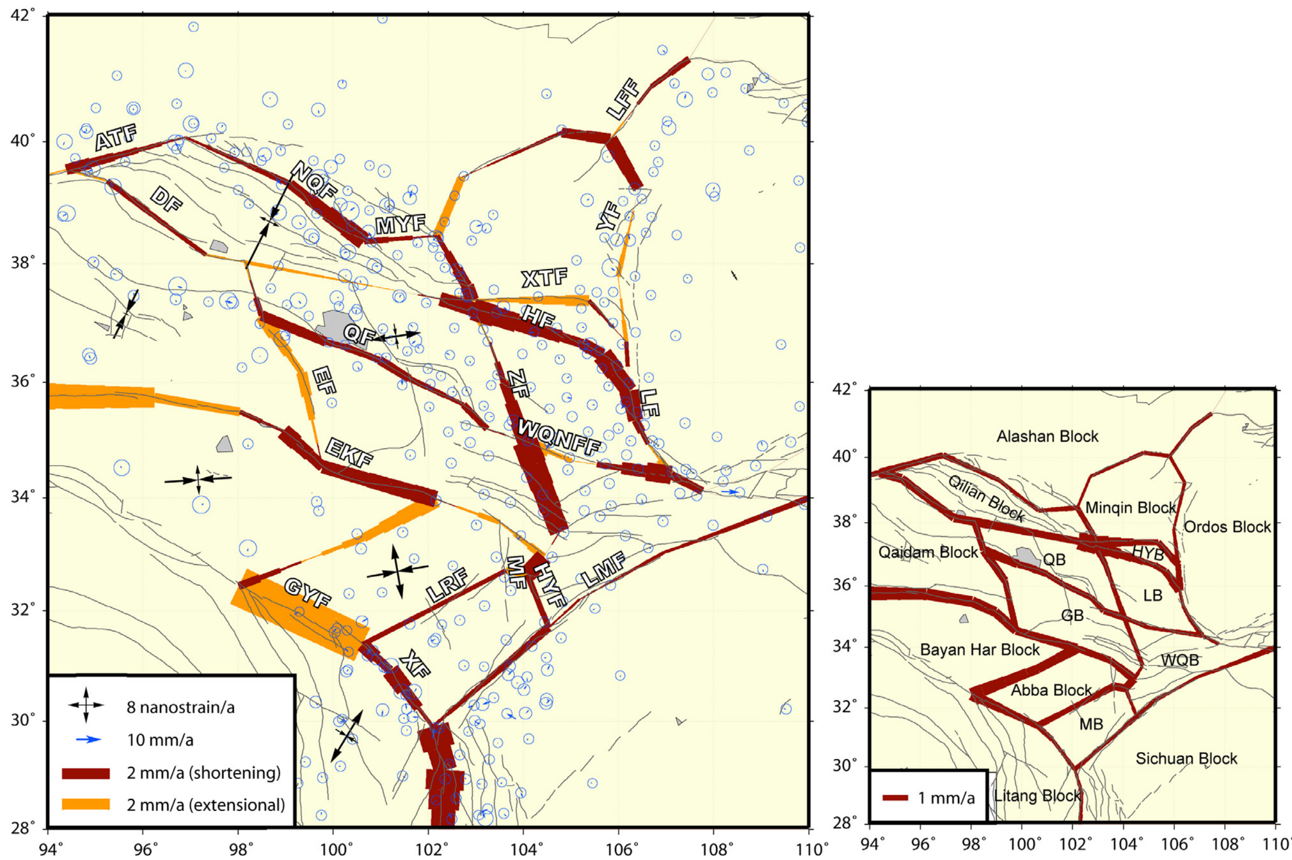

Fig. 6. Inversion results of DBM. The left panel shows strain rates within the seven blocks found to be internally deforming and normal-slip rates across faults. The crossed arrows are the strain rates, whose values are listed in Table 2. The right panel shows the uncertainties of fault normal slip rates.

6. Seismic moment accumulation rate

We measure strain energy accumulation rates within blocks and along their boundaries, and convert them to seismic moment accumulation rates. For strain energy within blocks, the seismic moment accumulation rate is the product of the strain rate, block volume, and the crustal shear modulus for the block interior. For strain energy along block boundaries, it is the product of the fault slip rate, the area of the fault plane above the locking depth, and the crustal shear modulus of the fault. Assuming geodetically derived seismic moment accumulation will eventually be released by earthquakes, these seismic moment accumulation rates provide important information for assessment of the seismic moment budget within and along the boundaries of blocks.

Seismic moment accumulation rate along block boundaries can be written in the following form:

$$\dot{M}_f = \dot{M}_p + \dot{M}_n, \tag{3}$$

where $\dot{M}_p = \mu L d v_p$, which is the seismic moment accumulation rate for the strike-slip component. The shear modulus of crust μ is taken to be 3×10^{10} Pa in our study. L and d are the length and locking depth (i.e. 20 km as assumed above) of the fault, respectively, and v_p is the strike-slip rate of the fault. $\dot{M}_n = \sqrt{2}\mu L d v_n$ is the seismic moment accumulation rate for the normal component. v_n is the convergence/extension rate, which is equivalent to dip slip rate assuming a listric fault, and $\sqrt{2}Ld$ is the locking area of the fault plane assuming a dip angle of 45°.

In order to estimate the seismic moment accumulation rate within blocks, we first need to determine faulting styles under which the strain energy would be released eventually during seismic events. For a given fault style, we can decompose the strain rate tensor into two or three simple components through coordinate transformation, each of which is equivalent to a double-couple dislocation source. The seismic moment accumulation rate within a given block is the sum of seismic moment accumulation rates associated with all of the double-couple dislocation sources. Different decompositions of the strain rate tensor would result in somewhat different estimates of seismic moment accumulation rate.

Assuming that the crust media is incompressible, the strain tensor is as follows under the free-surface condition:

$$\begin{bmatrix} \varepsilon_{11} & \varepsilon_{12} & 0 \\ \varepsilon_{21} & \varepsilon_{22} & 0 \\ 0 & 0 & -\Delta \end{bmatrix},$$

where $\Delta = \varepsilon_{11} + \varepsilon_{22} = \varepsilon_1 + \varepsilon_2$, and ε_1 and ε_2 are the two horizontal principal components. Savage and Simpson (1997) suggested three ways to decompose the tensor into two sub-tensors:

$$\begin{bmatrix} \varepsilon_{11} & \varepsilon_{122} & 0 \\ \varepsilon_{21} & \varepsilon_{22} & 0 \\ 0 & 0 & -\Delta \end{bmatrix} \rightarrow \begin{bmatrix} \varepsilon_1 & 0 & 0 \\ 0 & -\varepsilon_1 & 0 \\ 0 & 0 & 0 \end{bmatrix} + \begin{bmatrix} 0 & 0 & 0 \\ 0 & \Delta & 0 \\ 0 & 0 & -\Delta \end{bmatrix} \tag{4}$$

$$\begin{bmatrix} \varepsilon_{11} & \varepsilon_{122} & 0 \\ \varepsilon_{21} & \varepsilon_{22} & 0 \\ 0 & 0 & -\Delta \end{bmatrix} \rightarrow \begin{bmatrix} -\varepsilon_2 & 0 & 0 \\ 0 & \varepsilon_2 & 0 \\ 0 & 0 & 0 \end{bmatrix} + \begin{bmatrix} \Delta & 0 & 0 \\ 0 & 0 & 0 \\ 0 & 0 & -\Delta \end{bmatrix} \tag{5}$$

$$\begin{bmatrix} \varepsilon_{11} & \varepsilon_{122} & 0 \\ \varepsilon_{21} & \varepsilon_{22} & 0 \\ 0 & 0 & -\Delta \end{bmatrix} \rightarrow \begin{bmatrix} \varepsilon_1 & 0 & 0 \\ 0 & 0 & 0 \\ 0 & 0 & -\varepsilon_1 \end{bmatrix} + \begin{bmatrix} 0 & 0 & 0 \\ 0 & \varepsilon_2 & 0 \\ 0 & 0 & -\varepsilon_2 \end{bmatrix} \tag{6}$$

The decompositions shown in formulae (4)–(6) share some common features, i.e. each solution is decomposed into two double-couple sources, with one corresponding to a pure thrust/normal fault dipping at 45°, and the other a vertical strike-slip fault whose strike direction rotates 45° from the horizontal principal strain directions. Following Kostrov (1974), the corresponding scalar moment of the three decompositions can be written as

$$M_0^1 = 2\mu Sd(|\varepsilon_1| + |\Delta|) \tag{7}$$

$$M_0^2 = 2\mu Sd(|\varepsilon_2| + |\Delta|) \tag{8}$$

$$M_0^3 = 2\mu Sd(|\varepsilon_1| + |\varepsilon_2|) \tag{9}$$

where μ is the shear modulus, S is the area within a block, and d is the seismogenic depth.

Savage and Simpson (1997) recommended using the following definition to make sure that the components of both resolved double-couple tensors have the same algebraic sign as the corresponding component of the strain tensor:

$$M_0^S = 2\mu Sd\mathrm{Max}(|\varepsilon_1|, |\varepsilon_2|, |\varepsilon_1 + \varepsilon_2|) \tag{10}$$

where $\mathrm{Max}(|\varepsilon_1|, |\varepsilon_2|, |\varepsilon_1 + \varepsilon_2|)$ is equal to the largest of $|\varepsilon_1|$, $|\varepsilon_2|$, and $|\varepsilon_1 + \varepsilon_2|$.

Ward (1994) chose to use:

$$M_0^W = 2\mu Sd\mathrm{Max}(|\varepsilon_1|, |\varepsilon_2|) \tag{11}$$

for seismic moment calculation, where $Max(|\varepsilon_1|, |\varepsilon_2|)$ is equal to the lager of $|\varepsilon_1|$ and $|\varepsilon_2|$. The Working Group on California Earthquake Probabilities (1995) used the following definition:

$$M_0^{WG} = 2\mu Sd|\varepsilon_1 - \varepsilon_2| \tag{12}$$

Though the decompositions of formulae (4)–(6) have clear physical meanings that the resolved matrices are equivalent to double-couples on two non-parallel faults, it does not seem to be physically likely that tectonic deformation in the real world would be partitioned in such a way. It is more natural and acceptable for a tectonic deformation field to be partitioned between two parallel or sub-parallel faults, among which one is with pure shear and the other with pure normal/thrust motion. This is supported by many observations of parallel faults at oblique subduction zones, such as at the Sumatra, Philippines, and Hikurangi subduction zones (e.g. McCaffrey, 1992; Webb and Anderson, 1998; McCaffrey et al., 2000). Although we do not know exactly how the seismic moment accumulated in each block would be released, we consider the uniform strain rate within blocks as the virtual integration of deformation associated with intra-block minor faults, and speculate the deformation to be partitioned in that way. Therefore we choose the following decomposition scheme (the detailed derivation is stated in Appendix A):

$$\begin{bmatrix} \dot{\varepsilon}_1 & 0 & 0 \\ 0 & \dot{\varepsilon}_1 & 0 \\ 0 & 0 & -\dot{\Delta} \end{bmatrix} \rightarrow \begin{bmatrix} \dot{\Delta} & 0 & 0 \\ 0 & 0 & 0 \\ 0 & 0 & -\dot{\Delta} \end{bmatrix} + \begin{bmatrix} 0 & \sqrt{-\dot{\varepsilon}_1\dot{\varepsilon}_2} & 0 \\ \sqrt{-\dot{\varepsilon}_1\dot{\varepsilon}_2} & 0 & 0 \\ 0 & 0 & 0 \end{bmatrix} \tag{13}$$

This decomposition corresponds to two double couple dislocation sources with their fault planes sharing a common strike.

Accordingly, the seismic moment accumulation rate inferred for the block can be written in the following form based on the Kostrov's (1974) formula:

$$\dot{M}_b = \dot{M}_1 + \dot{M}_2, \tag{14}$$

where $\dot{M}_1 = 2\mu Sd\dot{\Delta}$, $\dot{M}_2 = 2\mu Sd\sqrt{-\dot{\varepsilon}_1\dot{\varepsilon}_2}$.

Since our aim is to investigate the deformation pattern of the studied region, it should be more robust to estimate a total seismic moment accumulation rate for all the blocks or block boundaries than just for an individual block or block boundary. Following Eqs. (3) and (14) we estimate the total moment accumulation rate within and along the boundaries of the blocks respectively. Blocks with portions located outside of the studied region, such as the Alashan, Ordos, Sichuan, and Litang blocks, are not accounted for in the moment accumulation estimation. The only exception is the Qaidam block, as it is located within the northeastern Tibetan plateau and most of the block is within the studied region, with enough GPS data for a reliable estimation of its block motion and boundary slip. Since no slip rate estimate is obtained for the southern boundary of the Bayan Har block, i.e. the Yushu-Fenghuoshan fault, we use the strike slip rate of 6.1–6.6 mm/a reported by Wang et al. (2013) to calculate its seismic moment accumulation rate. The area of each block accounts only the interior part, i.e. a margin of 8 km width is trimmed off (how the value is determined is described in the following paragraph), to be consistent with the way the seismic moment release rate is estimated in the following section. The seismic moment accumulation rate along block boundaries is divided equally between the two blocks. The moment accumulation rates within and along boundaries of blocks are thus determined as ~8.40×10^{18} N·m/a and ~2.06×10^{19} N·m/a, respectively.

7. Seismicity and seismic moment release rate

In order to compare the geodetic deformation field with seismicity, we further perform a statistical analysis of a joint earthquake catalog of historical (Gu, 1983) and modern (http://www.csndmc.ac.cn/newweb/data.htm) earthquakes. Owing to finite widths and non-vertical dip angles of fault zones and the uncertainties of earthquake locations, we first determine the horizontal width of a fault zone by investigating spatial distribution of regional earthquakes. If the horizontal extent of a fault zone is defined as a span within which more earthquakes occurred (or higher density of seismic moment released) than outside, the cumulative seismic moment released by earthquakes located within a certain range (w) from a given block boundary will increase along with

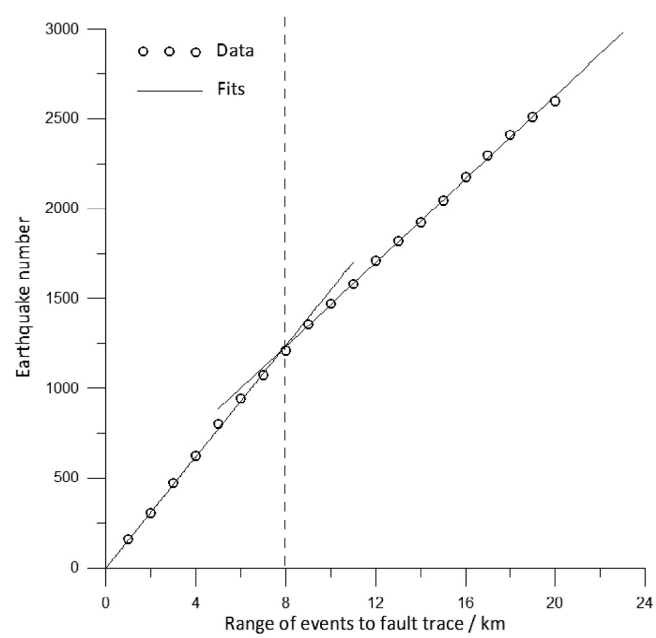

Fig. 7. Relationship of cumulative earthquake number vs range of events to fault trace.

w, and the increasing rate will taper down once *w* exceeds the width of the fault zone (w_0). Although this is not a precise definition of fault zone width, whose value is probably not well constrained or unique due to complexity of actual fault zone architecture etc., it turns out to be an effective way to discriminate earthquakes within and outside of fault zones and avoid having earthquakes within fault zones been accounted for intra-block seismic strain estimate. Since a relatively small number of strong earthquakes have released most of the total seismic moment, the statistical results based on seismic moment would be dominated by these strong earthquakes. Therefore, we test the relationship between the number of earthquakes occurring within a distance range *w* centered at the fault trace (i.e. the block boundaries) and the distance range *w*, shown in Fig. 7.

As seen in Fig. 7, the cumulative curve of earthquake count demonstrates two different trends for data segments close to and away from the fault trace. The intersection point of the two segments corresponds to half-width of the fault zone, which is 8 km. Earthquakes are therefore identified as occurring either within the 16-km-wide fault zones or in block interiors, the areal ratio between the two regions is 0.07:1.

As shown in Fig. 8, recorded earthquakes were scarce before 1550, more frequent after 1550, and soared considerably since 1920, when instrumental records became available. The catalog for M > 6 earthquakes is also found to become complete in the Qilian, Qinghai, and Qaidam regions (Huang et al., 1994). We therefore use the catalog since 1920 to estimate the seismic moment release rate.

To convert the earthquake magnitude into seismic moment we use the following relationship which was obtained by least-squares fitting of a linear relationship between the earthquake magnitudes of $M \geq 6.0$ events in the Chinese earthquake catalog and the logarithmic of seismic moments (Wang et al., 2009):

$$\mathrm{Log}\, M_0 = 7.5967 + 1.6073 M_s \tag{15}$$

The seismic moments released within block interiors and fault zones are then estimated as 5.76×10^{19} and 2.32×10^{20} N·m respectively during the time period of 1920–2015. The average seismic moment release rates are therefore estimated as 6.06×10^{18} and 2.44×10^{19} N·m/a for within the block interiors and the fault zones during this period.

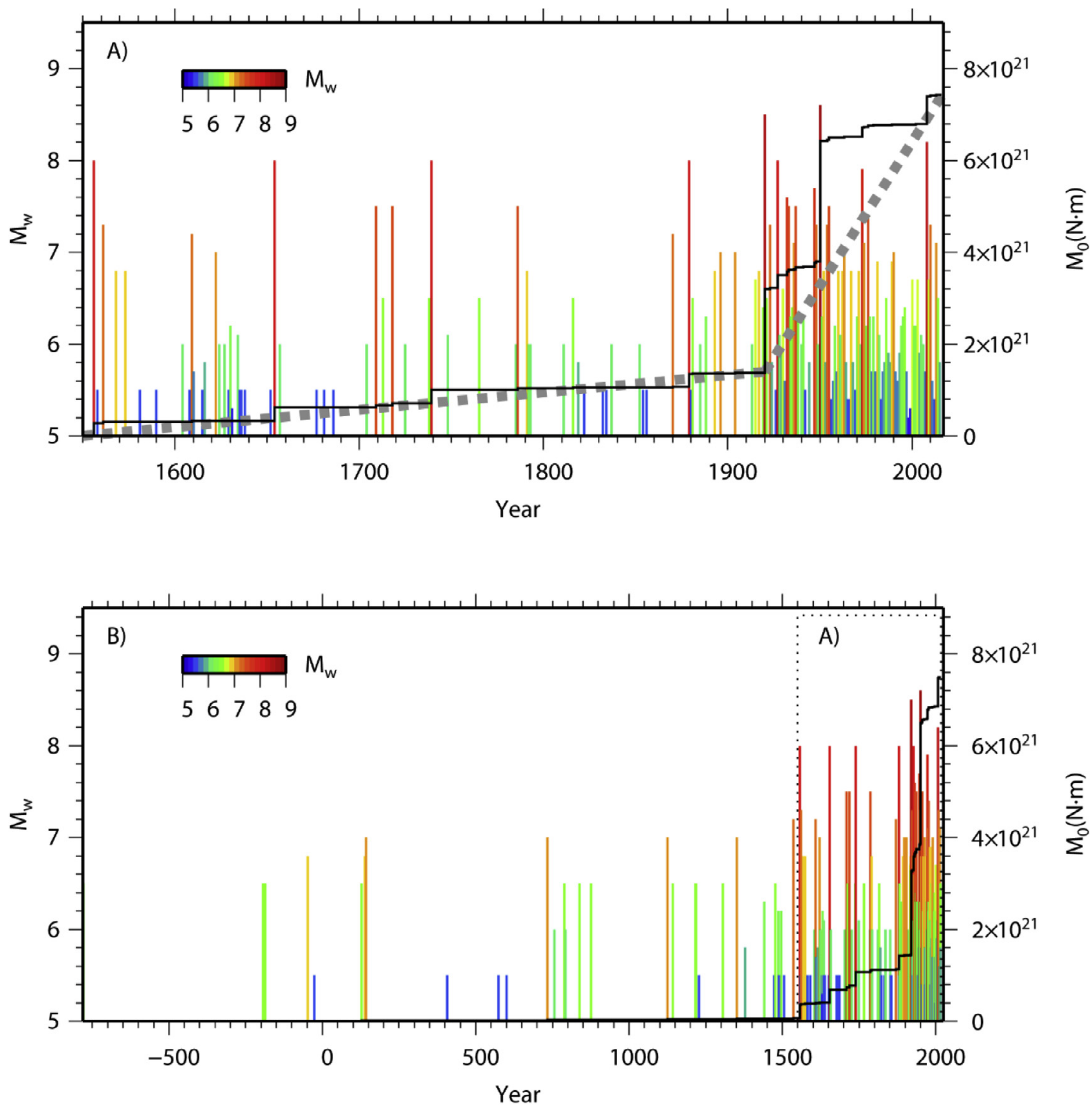

Fig. 8. Temporal distribution of earthquake catalog. Panels (A) and (B) show the data for 780 BCE–2015 and 1550–2015 respectively. Vertical bars indicate cumulative seismic moment release in each year in units of moment magnitude. Black curves denote accumulated seismic moment release since the starting time in the unit of N·m. Grey dash lines in panel (A) delineate average release rates of seismic moment during periods of 1550–1920 and 1920–2015, respectively.

8. Model comparisons

Comparing our model with the one developed by Loveless and Meade (2011), we find many similarities but also some remaining differences. The major differences are (as shown in Fig. S2): (1) The Wuwei and Yumushan blocks are separated from the Minqin block, and merged into the Qilian and Alashan blocks respectively in our model based on the block independence test results. More stations located within the Yumushan and Wuwei blocks helped us better define the block boundaries between the Qilian, Alashan, and Minqin blocks. (2) The southern boundary of the Qilian block is set as the Holocene Danghenanshan fault rather than the Northern Qaidam fault, which, according to Deng et al. (2003), has not slipped in the Holocene. (3) Between the Minqin and Lanzhou blocks, a separate Haiyuan block is delineated with the Haiyuan and Xiangshan-Tianjingshan faults as its southern and northern boundaries, respectively. This block, although rather small, is verified to be independent from its neighbors via the statistical test. (4) The Xining and Hezuo blocks are merged into the Qinghai and Guinan blocks in our model, rather than the Lanzhou and West Qinling blocks in the Loveless and Meade's model, again based on the block independence tests. However, since the statistical independence of the Xining block from the Qinghai and Lanzhou blocks are not significantly different, with values of 63.2% and 87.1%, respectively, we do not rule out completely the Loveless and Meade's model geometry. (5) Inspect of the Northern Chengxian Basin fault, the northeastern extension of the Longmenshan fault is selected in our model as part of the northwestern boundary of the Sichuan block. (6) The Huya fault in our model is taken as the boundary between the Maerkang and West Qinling blocks, which is verified to be active (Wang and Shen, 2011). Discrepancies in boundary delineations of the Tianshui, West Qinling, Pingwu, and Maerkang blocks may result from fewer data points used by Loveless and Meade (2011) than that in our study in this area. (7) The Bayan Har block is separated from the Abba block by a NE-SW trending boundary, while this region is divided into two blocks by a NW-SE trending fault by Loveless and Meade (2011). Nevertheless, station coverage within the Ganzi-Xianshuihe sliver in the Loveless and Meade's model is too sparse to adequately define the block geometry there.

Consequently, it is no surprise for us to obtain slip rate estimates consistent with that of Loveless and Meade (2011) across most faults in the region. Nevertheless, there are still significant discrepancies across several faults: (1) the WQNF fault is estimated to slip at much lower rate in our model. Compared with our model, GPS stations located south of the WQNF fault in the model of Loveless and Meade (2011) are much fewer (10 vs >20 in a similar range) and more unevenly distributed, making their estimation more prone to be biased by outliers. (2) We obtain a slip rate which is ~3 mm/a higher than their estimate across the Xianshuihe fault. This discrepancy could be mainly due to difference in estimating the Longmenshan block motion rate. Their estimate of the block motion rate seemed to have incorporated a station velocity outlier in the dataset, resulting in a more southeastward motion of the block than that of ours, and an underestimated sinistral slip across the Xianshuihe fault by ~3 mm/a. (3) We obtain lower and higher slip rates across the Longmenshan and Longriba faults respectively. The difference in the Longmenshan fault slip rate estimate is caused by the discrepancy in estimate of the Longmenshan block motion rate as mentioned above. A slightly higher slip rate estimate across the Longriba fault may be due to the deformation tradeoff between the Longmenshan and Longriba faults. (4) our estimation of the slip rate across the northeastern segment of the Altyn Tagh fault is lower than that of Loveless and Meade (2011). Such difference, however, is acceptable because the slip rate is estimated in the range of 91–97°E in their model and 94.5–97°E in our model respectively and it has been revealed that slip rate decreases northeastward along the Altyn Tagh fault.

Loveless and Meade (2011) also assessed internal deformation within blocks, and tested significance of internal deformation above data noise using a Monte Carlo statistical approach. Our study agrees with theirs in that there is insignificant internal deformation of blocks located outside of the plateau, but disagrees with theirs on the internal deformation of blocks located within the plateau. Loveless and Meade (2011) found no distinguishable internal deformation within any of the blocks except a sliver block north of the Ganzi-Yushu fault, and we infer that most of the blocks in the northeastern plateau have significant internal deformation. The discrepancy is not in the amount of internal deformation measured – Loveless and Meade (2011) derived homogeneous deformation within the blocks, which could even be higher than our estimates – but their Monte Carlo tests showed that these estimates cannot be distinguished from noise. The issue therefore becomes which way would be more reliable to test the significance of the solution for internal deformation. The Monte Carlo simulations that Loveless and Meade (2011) incorporated rely on GPS data uncertainties to define the noise level locally. These uncertainties were used to weight the data fitting residual χ^2s, but without taking into account the covariances between velocities (such covariances were not provided in the dataset they used). The GPS velocity solutions they used are referenced to the stable part of the Eurasia plate, which is located thousands of kilometers away from the region; and the data uncertainties are therefore relatively large. Without taking into account the covariances (which are large between local velocities) the χ^2s evaluated would be much greater than they ought to be, resulting in inadequate accounting of the noise level (we know about this because the dataset used in their study (Gan et al., 2007) was produced by our group). In our statistical test we use the F-test instead, which accounts for the relative ratio of the postfit residual χ^2s rather than the χ^2s themselves, avoiding the issue of uncertainty scaling. The high confidence levels of our F-test results attest reliability of our estimation of the block internal deformation.

Both ours and Loveless and Meade's model are quite different from that of Thatcher (2007), which adopts a much simpler block geometry based on limited GPS station coverage in his study. As shown in Fig. S2, the northeast Tibet block in his model is further decomposed into the Qinghai, Lanzhou, Guinan, West Qinling, and northern part of the Qaidam blocks in our model, and the south Tibet block in his model is decomposed into the Bayan Har, Abba, and northwestern part of the Maerkang blocks in our model, respectively.

We use a series of F-tests to determine whether a region should be described as one block or divided into several blocks. Zhang and Wei (2011) dealt with the issue using a somewhat different approach, called the K-means clustering method. Although this approach is effective in grouping the data, it is not explicit in taking into account the geographic locations of the data points with respect to fault traces and is therefore not so effective in identifying the right block boundaries. We made individual tests of the sites located near the block borders using the F-test and investigated velocity profiles across faults, and therefore would not have such a problem.

9. Discussion

The estimated internal strain rates are less than 3 nanostrain/a for blocks located outside of the Tibetan plateau, such as the Alashan, Minqin, Ordos, and Sichuan blocks. Except for the Ordos block, F-test results show that the significance of such internal deformation are lower than 70% (internal deformation within the Ordos block is significant but still very small). For blocks located within the plateau, on the other hand, the magnitudes of their estimated strain rates are much higher, ranging from 5 to 15 nanostrain/a. The significances of their internal deformation range from 66.6% to 99%. Most blocks with lower confidence levels either are relatively small blocks or have fewer GPS velocities. We therefore conclude that blocks located within the plateau in general have much stronger internal deformation than those located outside.

Though occupying only 6.5% of the total area, $\sim$71% of the seismic moment was accumulated and $\sim$80% of seismic moment was released within the fault zones in the past 95 years. The strain energy is therefore primarily accumulated and released in the block boundary zones, with a minor but still significant portion within block interiors. In addition, we also note that the seismic moment release rates are $\sim$118% and $\sim$72% of the seismic moment accumulation rates inside and outside of the fault zones, respectively. A ratio of $\sim$63% between seismic moment release and accumulation rates at block boundaries has been estimated by Wang et al. (2009) using a rigid block model and an earthquake catalog during the period of 1879–2007 in the Songpan-Ganzi region. Both estimates indicate comparable accumulation and release rates of seismic moment. Deficit between release and accumulation rates of seismic moment in their study may due to an incomplete earthquake catalog. The reasons for a higher/lower release rate of seismic moment within and outside of the fault zones compared with the corresponding accumulation rate could be: (a) the fault zone width in this paper for separating earthquakes within fault zones from those outside might be overestimated, (b) the fault locking depths at block boundaries might be greater and/or the elastic thickness of lithosphere within blocks might be smaller than 20 km as assumed, (c) a certain portion of the seismic moment was released aseismically within blocks, and (d) the occurrence of earthquakes is clustered, the 95-year record is significantly shorter than the full recurrence intervals.

Collision between the India and Asia plates caused wide spread lithospheric deformation in and around the Tibetan plateau. The resultant deformation pattern, however, varies considerably and is subject to the lithospheric strength. The integrated strength of the lithosphere beneath the Ordos, Sichuan Basin, and Qaidam blocks are inferred to be higher than that beneath the region approximately embracing the Qilian, Haiyuan, Qinghai, and Lanzhou blocks, due to differences in crustal composition, tectonic strain rate, and thermal structure derived from heat flow measurements (Tapponnier et al., 2001; Shen et al., 2003; Zhang et al., 2004; Yao et al., 2010; Wei et al., 2001; Wang, 2001). This is also supported by the regional seismicity observations, which indicate that most earthquakes within the Tibetan plateau occur at depths of less than 20 km except underneath the Qaidam basin (Liu et al., 2011a,b; Sun et al., 2006; Wang et al., 2000; Xin et al., 2010; Yang et al., 2003; Zhu et al., 2012), where some events could reach depths down to 24 km (Sun et al., 2006). On the other hand, the earthquakes underneath the Ordos block reach down to 29 km or even deeper (Wang et al., 2000), and the deepest ones underneath the Sichuan basin occur as deep as of $\sim$40 km (Yang et al., 2003). This seismicity distribution is directly related to effective elastic plate thickness across the Tibet (Braitenberg et al., 2003; Hetényi et al., 2006; Jiang and Jin, 2005). As a result, lower crustal materials within regions surrounding the Tibetan plateau seem to be more brittle and therefore stronger than the lower crustal materials within the plateau; and under the tectonic loading stress, the region within Tibet has broken up into multiple blocks of smaller-scales with significant internal deformation in contrast to the region surrounding the plateau.

With respect to the Alashan block, the Ordos block, pushed by blocks at its southwest rim, shows a counter-clockwise rotation of 9.1 nanorad/a, the Sichuan basin moves east-southeastward at 9.4 mm/a under the push of blocks to its west and northwest rim; the Qaidam, Bayan Har, Qilian, West Qinling, and Maerkang blocks rotate counterclockwise, while the Qinghai, Lanzhou, Haiyuan, Guinan, and Abba blocks rotate clockwise, respectively (Fig. 5). Mandl (1987) and Guo et al. (2000) suggested that the blocks bounded by a group of WNW-trending sinistral faults and a group of NNW-trending dextral faults should deform in a bookshelf style with counterclockwise rotation. This suggestion, however, disagrees with the rotation pattern of the blocks located mainly in the east part of this region. The crust here manifests not only regional sinistral shear, but also a northeastward push from crustal material to the southwest. The northeastward push is blocked by the Alashan, Minqin, and Ordos blocks to the north and east, causing the blocks in the east region to rotate clockwise and escape southeastward at the eastern boundary.

Chang et al. (2008), McNamara et al. (1994), Sol et al. (2007) and Fu et al. (2008) found that the fast shear wave directions within our studied region change from ENE in the southwest to ESE in the northeast, and SE in the south, which is consistent with the clockwise rotation pattern of the GPS velocity field. We infer that the motion of the upper crust in the studied region might be driven by flow in the lithosphere or asthenosphere.

10. Conclusion

Resisted by the stable Alashan and Ordos blocks in the north and northeast, the northeastern margin of the Tibetan plateau demonstrates a clockwise rotation and moves from northeastward to southeastward toward the Sichuan basin, resulting in strain accumulation across the Longmenshan range and the southeastward movement of the Sichuan Basin. This is realized by transpressional deformation with a sinistral component across most of the WNW-trending faults and dextral deformation across most of the NNW-trending faults, respectively.

The sinistral slip rates are estimated across the Northern Qilian (1.1 ± 1.0 mm/a), Danghenanshan (2.8 ± 1.7 mm/a), Haiyuan (4.3 ± 1.6 mm/a across its western segment and 4.6 ± 1.8 mm/a across its eastern segment), Qinghainanshan (2.4 ± 1.2 mm/a), WQNF (1.3 ± 1.0 mm/a), East Kunlun (10.8 ± 2.3 mm/a across its western segment, 4.6 ± 2.6 mm/a across its central segment, and 3.8 ± 2.1 mm/a across its eastern segment), Ganzi-Yushu (10.4 ± 2.1 mm/a across its southeastern segment), and Xianshuihe (14.3 ± 1.6 mm/a) faults. Right-lateral slip at a rate of 3.5 ± 1.7 mm/a is estimated across most part of the NNW-trending Elashan fault. The NE-trending Altyn Tagh fault slips left laterally on its easternmost segment at a rate of 1.3 ± 1.4 mm/a, and the southwestern, central, and northeastern segments of the Longmenshan fault slip right laterally at rates of 1.7 ± 1.1, 1.1 ± 0.8, and 1.1 ± 0.8 mm/a, with shortening rates of 1.1 ± 1.2, 0.4 ± 0.8, and 0.8 ± 1.1 mm/a respectively. The Longriba fault slips right laterally at a rate of 4.9 ± 1.5 mm/a.

The studied region is divided by these faults into 15 blocks, whose deformation is neither consistent with the "rigid block" nor the "continuous deformation" hypothesis, but partitioned between relative motion among blocks of about 100 km in scale and internal deformation on the order of 10 nanostrain/a within the blocks. Assuming a 20-km fault locking depth, the geodetically determined seismic moment accumulation rates inside the blocks and at the block boundaries are 8.40×10^{18} and 2.06×10^{19} N·m/a, respectively. Our analysis of the earthquake catalog during the time period of 1920–2015 indicates average seismic moment release rates of 6.06×10^{18} and 2.44×10^{19} N·m/a within block interiors and at block boundary zones, respectively. These results suggest that the relative distribution of seismic and deformation intensities between inside and outside of the block boundary zones are similar, about 80% vs. 20% for moment release and 71% vs. 29% for moment accumulation, respectively. Distributed low velocity zones and shallower seismogenic depth detected underneath the eastern Tibetan plateau suggest that the rheological structure of the crust and lithosphere plays an important role in restricting the deformation style of the region, which is located at the frontier of the eastward extrusion of the Tibetan plateau.

Acknowledgements

The authors are grateful to Mingjie Xu, Xiwei Xu, Qidong Deng, Jiangning Lu, Wei Tao, Yongge Wan, and Roland Bürgmann for their helpful suggestions and discussion. We also thank the editors, reviewer Jeff Freymueller, and an anonymous reviewer for their thoughtful and constructive reviews and suggestions. This work was supported by the National Natural Science Foundation of China (41474028, 41090294 and 41104008), the China Earthquake Administration (200708002), and the US National Science Foundation (EAR-1323052).

Appendix A

In a principal cartesian coordinate system of xyz, the strain rate matrix is in the form:

$$\begin{bmatrix} \dot{\varepsilon}_1 & 0 & 0 \\ 0 & \dot{\varepsilon}_2 & 0 \\ 0 & 0 & -\dot{\Delta} \end{bmatrix}.$$

In a new coordinate system of x′y′z where x′ and y′ are new axes rotated by an angle α from the x and y axes in the x-y plane, the strain rate tensor becomes:

$$\begin{bmatrix} \dot{\varepsilon}_{11} & \dot{\varepsilon}_{12} & 0 \\ \dot{\varepsilon}_{21} & \dot{\varepsilon}_{22} & 0 \\ 0 & 0 & -\dot{\Delta} \end{bmatrix},$$

where

$$\dot{\varepsilon}_{11} = \frac{1}{2}(\dot{\varepsilon}_1 + \dot{\varepsilon}_2) + \frac{1}{2}(\dot{\varepsilon}_1 - \dot{\varepsilon}_2) \cdot \cos 2\alpha \tag{A.1}$$

$$\dot{\varepsilon}_{12} = \dot{\varepsilon}_{21} = \frac{1}{2}(\dot{\varepsilon}_1 - \dot{\varepsilon}_2) \cdot \sin 2\alpha \tag{A.2}$$

$$\dot{\varepsilon}_{22} = \frac{1}{2}(\dot{\varepsilon}_1 + \dot{\varepsilon}_2) - \frac{1}{2}(\dot{\varepsilon}_1 - \dot{\varepsilon}_2) \cdot \cos 2\alpha \tag{A.3}$$

In order to decompose the strain rate tensor into two double-couple dislocation components with their fault planes sharing a common strike, the two components need to be one strike-slip and the other dip-slip, and one of the horizontal diagonal terms needs to be zero. Let $\dot{\varepsilon}_{22}$ be zero, and we get $\alpha = \frac{1}{2}\arccos\left(\frac{\dot{\varepsilon}_1+\dot{\varepsilon}_2}{\dot{\varepsilon}_1-\dot{\varepsilon}_2}\right)$. Accordingly, Eqs (A.1)–(A.3) become

$$\dot{\varepsilon}_{11} = \dot{\varepsilon}_1 + \dot{\varepsilon}_2 = \dot{\Delta} \tag{A.4}$$

$$\dot{\varepsilon}_{12} = \sqrt{-\dot{\varepsilon}_1\dot{\varepsilon}_2} \tag{A.5}$$

$$\dot{\varepsilon}_{22} = 0 \tag{A.6}$$

By substituting Eqs (A.4)–(A.6) into the strain rate tensor in the new coordinate system, we get

$$\begin{bmatrix} \dot{\Delta} & \dot{\varepsilon}_{12} & 0 \\ \dot{\varepsilon}_{12} & 0 & 0 \\ 0 & 0 & -\dot{\Delta} \end{bmatrix} = \begin{bmatrix} \dot{\Delta} & 0 & 0 \\ 0 & 0 & 0 \\ 0 & 0 & -\dot{\Delta} \end{bmatrix} + \begin{bmatrix} 0 & \dot{\varepsilon}_{12} & 0 \\ \dot{\varepsilon}_{12} & 0 & 0 \\ 0 & 0 & 0 \end{bmatrix} \tag{A.7}$$

The tensor on the left-hand side of Eq. (A.7) has the same structure as that derived by Savage and Simpson (1997) assuming a fault system composed of two parallel faults with one dip-slip and another strike-slip. The first term on the right-hand side of Eq. (A.7) has two diagonal elements with the same magnitude but opposite signs in the x′z plane, which is equal to a pure dip-slip double-couple dislocation source with one fault plane striking in y′-direction and dipping at an angle of 45°. The second term is corresponding to a pure strike-slip double-couple dislocation source with one fault plane striking in y′-direction and dipping at 90°. Accordingly, the seismic moment accumulation rate can be written in the following form based on the Kostrov's (1974) formula:

$$\dot{M}_b = \dot{M}_1 + \dot{M}_2, \tag{A.8}$$

where $\dot{M}_1 = 2\mu Sd\dot{\Delta}$, $\dot{M}_2 = 2\mu Sd\dot{\varepsilon}_{12}$.

Appendix B. Supplementary material

Supplementary data associated with this article can be found, in the online version, at http://dx.doi.org/10.1016/j.jseaes.2017.02.040.

References

Allen, C.A., Luo, Z., Qian, H., Wen, X., Zhou, H., Huang, W., 1991. Field study of a highly active fault zone: the Xianshuihe fault of southwestern China. Geol. Soc. Am. Bull. 103 (9), 1178–1199. http://dx.doi.org/10.1130/0016-7606.

Avouac, J.P., Tapponnier, P., 1993. Kinematic model of active deformation in central Asia. Geophys. Res. Lett. 20 (10), 895–898.

Bilham, R., Larson, K., Freymueller, J., Idylhim, P., 1997. GPS measurements of present-day convergence across the Nepal Himalaya. Nature 386, 61–64.

Bird, P., 2003. An updated digital model of plate boundaries. Geochem. Geophys. Geosyst. 4 (3), 1027. http://dx.doi.org/10.1029/2001GC000252.

Braitenberg, C., Wang, Y., Fang, J., Hsu, H.T., 2003. Spatial variations of flexure parameters over the Tibet-Quinghai plateau. Earth Planet. Sci. Lett. 205 (3), 211–224.

Burchfiel, B.C., Zhang, P.Z., Wang, Y.P., Zhang, W.Q., Song, F.M., Deng, Q.D., Molnar, P., Royden, L., 1991. Geology of the Haiyuan fault zone, Ningxia-Hui autonomous region, China, and its relation to the evolution of the northeastern margin of the Tibetan Plateau. Tectonics 10 (6), 1091–1110.

Cavalié, O., Lasserre, C., Doin, M.P., Peltzer, G., Sun, J., Xu, X., Shen, Z.K., 2008. Measurement of interseismic strain across the Haiyuan fault (Gansu, China), by InSAR. Earth Planet. Sci. Lett. 275 (3–4), 246–257.

Chang, L.J., Wang, C.Y., Ding, Z.F., 2008. Seismic anisotropy of upper mantle in Sichuan and adjacent regions. Sci. China (Ser. D) 38 (12), 1589–1599.

Chen, J.H., Liu, Q.Y., Li, S.C., Guo, B., Lai, Y.G., 2005. Crust and upper mantle S-wave velocity structure across the northeastern Tibetan Plateau an Ordos block. Chin. J. Geophys. 48 (2), 333–342.

Chen, Q., Freymueller, J.T., Wang, Q., Yang, Z., Xu, C., Liu, J., 2004. A deformation block model for the present-day tectonics of Tibet. J. Geophys. Res. 109 (B01403). http://dx.doi.org/10.1029/2002JB002151.

d' Alessio, M.A., Johanson, I.A., Bürgmann, R., Schmidt, D.A., Murray, M.H., 2005. Slicing up the San Francisco Bay Area: block kinematics and fault slip rates from GPS-derived surface velocities. J. Geophys. Res. 110, B06403. http://dx.doi.org/10.1029/2004JB003496.

Deng, Q.D., Zhang, P.Z., Ran, Y.K., Yang, X.P., Min, W., Chu, Q.Z., 2003. Basic characteristics of active tectonics of China. Sci. China (Ser. D) 46, 356–372.

England, P., McKenzie, D., 1982. A thin viscous sheet model for continental deformation. Geophys. J. Int. 70 (2), 295–321.

England, P., Molnar, P., 1997. Active deformation of Asia: from kinematics to dynamics. Science 278 (5338), 647–650. http://dx.doi.org/10.1126/science.278.5338.647.

Feigl, K., Agnew, D.C., Bock, Y., Dong, D.N., Donnellan, A., Hager, B.H., Herring, T.A., Jackson, D.D., Jordan, T.H., King, R.W., Larsen, S., Larson, K.M., Murray, M.H., Shen, Z.K., Webb, F.H., 1993. Space geodetic measurement of crustal deformation in central and southern California, 1984–1992. J. Geophys. Res. 98 (B12), 21677–21712.

Flesch, L.M., Haines, A.J., Holt, W.E., 2001. Dynamics of the India-Eurasia collision zone. J. Geophys. Res. 106 (B8), 16435–16460.

Fu, Y.V., Chen, Y.J., Li, A., Zhou, S., Liang, X., Ye, G., Jin, G., Jiang, M., Ning, J., 2008. Indian mantle corner flow at southern Tibet revealed by shear wave splitting measurements. Geophys. Res. Lett. 35, L02308. http://dx.doi.org/10.1029/2007GL031753.

Gan, W.J., Zhang, P.Z., Shen, Z.K., Niu, Z.J., Wang, M., Wan, Y.G., Zhou, D.M., Cheng, J., 2007. Present-day crustal motion within the Tibetan Plateau inferred from GPS measurements. J. Geophys. Res. 112, B08416. http://dx.doi.org/10.1029/2005JB004120.

Gaudemer, Y., Tapponnier, P., Meyer, B., Peltzer, G., Guo, S., Chen, Z., Dai, H., Cifuentes, I., 1995. Partitioning of crustal slip between linked, active faults in

the eastern Qilian Shan, and evidence for a major seismic gap, the 'Tianzhu gap', on the western Haiyuan Fault, Gansu (China). Geophys. J. Int. 120 (3), 599–645.
Gu, G., 1983. Chinese Earthquake Catalog (1831 B.P.–1969 A.D.). Science Press, Beijing, China.
Guo, B., Liu, Q.Y., Chen, J.H., Liu, L.S., Li, S.C., Li, Y., Wang, J., Qi, S.H., 2004. Seismic tomographic imaging of the crust and upper mantle beneath the northeastern edge of the Qinghai-Xizang plateau and the Ordos area. Chin. J. Geophys. 47 (5), 790–797.
Guo, S.M., Jiang, Z.S., Zhang, C.L., 2000. Division and motion status of blocks for the northeastern Tibetan plateau in late Quaternary. Seismol. Geol. 22 (3), 219–231.
Herring, T.A., King, R.W., McClusky, S.C., 2010. GLOBK reference manual, Global Kalman filter VLBI and GPS analysis program, release 10.4. MIT Technical Reports, Cambridge, MA.
Hetényi, G., Cattin, R., Vergne, J., Nábělek, J.L., 2006. The effective elastic thickness of the India Plate from receiver function imaging, gravity anomalies and thermomechanical modelling. Geophys. J. Int. 1–15. http://dx.doi.org/10.1111/j.1365-246X.2006.03198.x.
Holt, W.E., Chamot-Rooke, N., Pichon, X.L., Haines, A.J., Shen-Tu, B., Ren, J., 2000. The velocity field in Asia inferred from Quaternary fault slip rates and GPS observations. J. Geophys. Res. 105, 19185–19210.
Houseman, G., England, P., 1986. Finite strain calculations of continental deformation 1. Method and general results for convergent zones. J. Geophys. Res. 91, 3651–3663.
Houseman, G., England, P., 1993. Crustal thickening versus lateral expulsion in the Indian-Asian continental collision. J. Geophys. Res. 98, 12233–12249.
Huang, J.L., Song, X.D., Wang, S.Y., 2003. Fine structure of Pn velocity beneath Sichuan-Yunan region. Sci. China (Ser. D) 33 (Suppl.), 144–150.
Huang, W.Q., Li, W.X., Gao, X.F., 1994. Research on completeness of earthquake data in the Chinese mainland (II)—the regional distribution of the beginning years of basically complete earthquake data. Acta Seismol. Sin. 7 (4), 529–538.
Institute of Geology, State Bureau of Seismology, Institute of Earthquake in Lanzhou, State Bureau of Seismology, 1993. Active Fault System in the Region of Qilian Mountain-Hexi Coridor. Seismological Press, Beijing, China.
Jiang, X., Jin, Y., 2005. Mapping the deep lithospheric structure beneath the eastern margin of the Tibetan Plateau from gravity anomalies. J. Geophys. Res. 110, B07407. http://dx.doi.org/10.1029/2004JB003394.
Kirby, E., Harkins, N., Wang, E.Q., Shi, X.H., Fan, C., Burbank, D., 2007. Slip rate gradients along the eastern Kunlun fault. Tectonics 26, TC2010. http://dx.doi.org/10.1029/2006TC002033.
Kostrov, V.V., 1974. Seismic moment and energy of earthquakes, and seismic flow of rock. Phys. Solid Earth 1, 12–21.
Lai, X., Zhang, X.K., Fang, S.M., 2004. Study of crust-mantle transitional zone along the northeast margin of Qinghai-Xizang plateau. Acta Seismol. Sin. 26 (2), 132–139.
Lasserre, C., Morel, P.H., Gaudemer, Y., Tapponnier, P., Ryerson, F.J., King, G.C.P., Mériaux, F., Kasser, M., Kashgarian, M., Liu, B.C., Lu, T.Y., Yuan, D.Y., 1999. Postglacial left slip rate and past occurrence of $M \geq 8$ earthquakes on the western Haiyuan fault, Gansu, China. J. Geophys. Res. 104 (B8), 17633–17651.
Lasserre, C., Gaudemer, Y., Tapponnier, P., Mériaux, A.S., Van der Woerd, J., Yuan, D. Y., Ryerson, F.J., Finkel, R.C., Caffee, M.W., 2002. Fast late Pleistocene slip rate on the Leng Long Ling segment of the Haiyuan fault, Qinghai, China. J. Geophys. Res. 107 (B11), 2276. http://dx.doi.org/10.1029/2000JB000060.
Lebedev, S., Nolet, G., 2003. Upper mantle beneath Southeast Asia from S velocity tomography. J. Geophys. Res. 108 (B1), 2048. http://dx.doi.org/10.1029/2000JB000073.
Li, C., Van der Hilst, R.D., Toksöz, M.N., 2006. Constraining P-wave velocity variations in the upper mantle beneath Southeast Asia. Phys. Earth Planet. Int. 154, 180–195.
Li, C.Y., Zhang, P.Z., Zhang, J.X., Yuan, D.Y., Wang, Z.C., 2007. Late-Quaternary activity and slip rate of the western Qinling fault zone at Huangxianggou. Quaternary Sci. 27 (1), 54–63.
Li, C., Van der Hilst, R.D., Meltzer, A.S., Engdahl, E.R., 2008. Subduction of the Indian lithosphere beneath the Tibetan Plateau and Burma. Earth Planet. Sci. Lett. 274, 157–168. http://dx.doi.org/10.1016/j.epsl.2008.07.016.
Li, C.Y., Zhang, P.Z., Yin, J.H., Min, W., 2009. Late Quaternary left-lateral slip rate of the Haiyuan fault, northeastern margin of the Tibetan Plateau. Tectonics 28, TC5010. http://dx.doi.org/10.1029/2008TC002302.
Li, C., 2005. Quantitative study on major active fault zones in northeastern Qinghai-Tibet Plateau Doctoral dissertation. Institute of Geology, China Earthquake Administration, Beijing, pp. 117–192.
Li, H., Van der Woerd, J., Tapponnier, P., Klinger, Y., Qi, X., Yang, J., Zhu, Y., 2005. Slip rate on the Kunlun fault at Hongshui Gou, and recurrence time of great events comparable to the 14/11/2011, Mw $\sim$ 7.9 Kokoxili earthquake. Earth Planet. Sci. Lett. 237, 285–299.
Li, Y., Xu, K., 2010. Discussion on the causative structure and relocation of the Oct. 25 2003 Minle-Shandan M 6.1 earthquake sequence. Seismol. Geomagn. Observation Res. 31 (2), 31–36.
Liu, M., Stein, S., Wang, H., 2011a. 2000 years of migrating earthquakes in North China: how earthquakes in midcontinents differ from those at plate boundaries. Lithosphere 3 (2), 128–132.
Liu, W., Wang, P., Ma, Y., Chen, Y., 2011b. Relocation of Dachaidan Ms 6.4 earthquake sequence in Qinghai province in 2009 using the double difference location method. Plateau Earthq. Res. 23 (1), 24–26.
Loveless, J.P., Meade, B.J., 2011. Partitioning of localized and diffuse deformation in the Tibetan Plateau from joint inversions of geologic and geodetic observations. Earth Planet. Sci. Lett. 303, 11–24.
Ma, H.S., Wang, S.Y., Pei, S.P., Liu, J., Hua, W., Zhou, L.Q., 2007. Q_0 tomography of S wave attenuation in Sichuan-Yunan and adjacent regions. Chin. J. Geophys. 50 (2), 465–471.
Mandl, G., 1987. Tectonic deformation by rotating parallel faults: The "bookshelf" mechanism. Tectonophysics 141, 277–316. http://dx.doi.org/10.1016/0040-1951(87)90205-8.
McCaffrey, R., 1992. Oblique plate convergence, slip vectors, and forearc deformation. J. Geophys. Res. 97 (B6), 8905–8915.
McCaffrey, R., Zwick, P.C., Bock, Y., Prawirodirdjo, L., Genrich, J.F., Stevens, C.W., Puntodewo, S.S.O., Subarya, C., 2000. Strain partitioning during oblique plate convergence in northern Sumatra: geodetic and seismologic constraints and numerical modeling. J. Geophys. Res. 105 (B12), 28363–28376.
McCaffrey, R., Qamar, A.I., King, R.W., Wells, R., Khazaradze, G., Williams, C.A., Stevens, C.W., Vollick, J.J., Zwick, P.C., 2007. Fault locking, block rotation and crustal deformation in the Pacific Northwest. Geophys. J. Int. 169, 1315–1340.
McNamara, D.E., Owens, T.J., Silver, P.G., Wu, F.T., 1994. Shear wave anisotropy beneath the Tibetan Plateau. J. Geophys. Res. 99 (B7), 13655–13665.
Meade, B.J., Hager, B.H., 2005. Block models of crustal motion in southern California constrained by GPS measurements. J. Geophys. Res. 110, B03403. http://dx.doi.org/10.1029/2004JB003209.
Mériaux, A.S., Tapponnier, P., Ryerson, F.J., Xu, X.W., King, G., Van der Woerd, J., Finkel, R.C., Li, H.B., Caffee, M.W., Xu, Z.Q., Chen, W.B., 2005. The Aksay segment of the northern Altyn Tagh fault: tectonic geomorphology, landscape evolution, and Holocene slip rate. J. Geophys. Res. 110, B04404. http://dx.doi.org/10.1029/2004JB003210.
Niu, Z., Wang, M., Sun, H., Sun, J., You, X., Gan, W., Xue, G., Hao, J., Xin, S., Wang, Y., 2005. Contemporary velocity field of crustal movement of Chinese mainland from Global Positioning System measurements. Chin. Sci. Bull. 50 (9), 939–941.
Okada, Y., 1992. Internal deformation due to shear and tensile faults in a half-space. Bull. Seismol. Soc. Am. 82 (2), 1018–1040.
Peltzer, G., Tapponnier, P., 1988. Formation and evolution of strike-slip faults, rifts, and basins during the India-Asia collision: an experimental approach. J. Geophys. Res. 93 (B12), 15085–15117.
Peltzer, G., Saucier, F., 1996. Present-day kinematics of Asia derived from geologic fault rates. J. Geophys. Res. 101 (B12), 27943–27956.
Reilinger, R.E., McClusky, S.C., Oral, M.B., King, R.W., Toksoz, M.N., Barka, A.A., Kinik, I., Lenk, O., Sanli, I., 1997. Global Positioning System measurements of present-day crustal movements in the Arabia-Africa-Eurasia plate collision zone. J. Geophys. Res. 102 (B5), 9983–9999.
Ren, J., Wang, M., 2005. GPS measured crustal deformation of the Ms 8.1 Kunlun earthquake on November 14th 2001 in Qinghai-Xizang plateau. Quaternary Sci. 25 (1), 34–43.
Replumaz, A., Tapponnier, P., 2003. Reconstruction of the deformed collision zone between India and Asia by backward motion of lithospheric blocks. J. Geophys. Res. 108 (B6), 2285. http://dx.doi.org/10.1029/2001JB000661.
Savage, J.C., 1983. A dislocation model of strain accumulation and release at a subduction zone. J. Geophys. Res. 88 (B6), 4984–4996.
Savage, J.C., Burford, R.O., 1973. Geodetic determination of relative plate motion in central California. J. Geophys. Res. 78 (5), 832–845.
Savage, J.C., Simpson, R.W., 1997. Surface strain accumulation and the seismic moment tensor. Bull. Seismol. Soc. Am. 87 (5), 1345–1353.
Shen, Z.K., Ge, B.X., Jackson, D.D., Potter, D., Cline, M., Sung, L.Y., 1996. Northridge earthquake rupture models based on the Global Positioning System measurements. Bull. Seismol. Soc. Am. 86, 37–48.
Shen, Z.K., Wang, M., Li, Y., Jackson, D.D., Fang, P., 2001. Crustal deformation along the Altyn Tagh fault system, western China, from GPS. J. Geophys. Res. 106 (B12), 30607–30621. http://dx.doi.org/10.1029/2001JB000349.
Shen, Z.K., Wang, M., Gan, W.J., Zhang, Z.S., 2003. Contemporary tectonics strain rate field of Chinese continent and its geodynamic implications. Earth Sci. Front. 10 (Suppl.), 94–100.
Shen, Z.K., Lü, J.N., Wang, M., Bürgmann, R., 2005. Contemporary crustal deformation around the southeast borderland of the Tibetan Plateau. J. Geophys. Res. 110 (11), B11409. http://dx.doi.org/10.1029/2004JB003421.
Shen, Z.-K., King, R., Agnew, D., Wang, M., Herring, T.A., Dong, D., Fang, P., 2011. A unified analysis of crustal motion in Southern California, 1970–2004: The SCEC Crustal Motion Map. J. Geophys. Res. 116, B11402. http://dx.doi.org/10.1029/2011JB008549.
Simpson, R.W., Thatcher, W., Savage, J.C., 2012. Using cluster analysis to organize and explore regional GPS velocities. Geophys. Res. Lett. 39 (L18307). http://dx.doi.org/10.1029/2012GL052755.
Sol, S., Meltzer, A., Bürgmann, R., Van der Hilst, R.D., King, R., Chen, Z., Koons, P.O., Lev, E., Liu, Y.P., Zeitler, P.Z., Zhang, X., Zhang, J., Zurek, B., 2007. Geodynamics of the southeastern Tibetan Plateau from seismic anisotropy and geodesy. Geology 35 (6), 563–566.
Sun, C., Qian, R., Xiao, G., Meng, X., 2006. The relocation and seismogenic structure of the Delingha earthquake sequence of 2003 in Qinghai. Geophys. Geochem. Explor. 30 (1), 79–82.
Tapponnier, P., Molnar, P., 1976. Slip-line field theory and large-scale continental tectonics. Nature 264 (5584), 19–24.
Tapponnier, P., Peltzer, G., Le Dain, A.Y., Armijo, R., Cobbold, P., 1982. Propagating extrusion tectonics in Asia: new insights from simple experiments with plasticine. Geology 10 (12), 611–616. http://dx.doi.org/10.1130/0091-7613.
Tapponnier, P., Xu, Z.Q., Roger, F., Meyer, B., Arnaud, N., Wittlinger, G., Yang, J.S., 2001. Oblique stepwise rise and growth of the Tibet Plateau. Science 294 (5547), 1671–1677.

Thatcher, W., 2007. Microplate model for the present-day deformation of Tibet. J. Geophys. Res. 112, B01401. http://dx.doi.org/10.1029/2005JB004244.
Van der Woerd, J., Ryerson, F.J., Tapponnier, P., Gaudemer, Y., Finkel, R., Mériaux, A. S., Caffee, M., Zhao, G., He, Q., 1998. Holocene left-slip rate determined by cosmogenic surface dating on the Xidatan segment of the Kunlun fault (Qinghai, China). Geology 26 (8), 695–698.
Van der Woerd, J., Ryerson, F.J., Tapponnier, P., Mériaux, A.S., Gaudemer, Y., Meyer, B., Finkel, R.C., Caffee, M.W., Zhao, G., Xu, Z., 2000. Uniform slip-rate along the Kunlun fault: implications for seismic behaviour and large-scale tectonics. Geophys. Res. Lett. 27 (16), 2353–2356.
Van der Woerd, J., Tapponnier, P., Ryerson, F.J., Mériaux, A.S., Meyer, B., Gaudemer, Y., Finkel, R.C., Caffee, M.W., Zhao, G., Xu, Z., 2002. Uniform postglacial slip-rate along the central 600 km of the Kunlun Fault (Tibet), from ^{26}Al, ^{10}Be, and ^{14}C dating of riser offsets, and climatic origin of the regional morphology. Geophys. J. Int. 148 (3), 356–388.
Vilotte, J.P., Daignières, M., Madariaga, R., 1982. Numerical modeling of intraplate deformation: simple mechanical models of continental collision. J. Geophys. Res. 87, 10709–10728.
Vilotte, J.P., Madariaga, R., Daignières, M., Zienkiewicz, O., 1986. Numerical study of continental collision: influence of buoyancy forces and an initial stiff inclusion. Geophys. J. Int. 84, 279–310.
Wallace, L.M., Beavan, J., McCaffrey, R., Darby, D., 2004. Subduction zone coupling and tectonic block rotations in the North Island, New Zealand. J. Geophys. Res. 109, B12406. http://dx.doi.org/10.1029/2004JB003241.
Wan, Y., Sheng, Z., Cheng, W., Zhang, Z., Wu, Y., Zhao, X., Bu, Y., Xue, Z., Liu, J., 2012. Earthquake location method with arrival time uncertainty considered and its application to location of earthquakes from 2001 to 2008 in Sichuan area. Seismol. Geol. 34 (1), 1–10.
Wang, F., Xu, X.W., Zheng, R.Z., 2003a. Slip rate of the eastern Alytn tagh fault since 20 ka BP. Seismol. Geol. 25 (3), 349–358.
Wang, H., Liu, M., Shen, X., Liu, J., 2009. Balance of seismic moment in the Songpan-Ganze region, eastern Tibet: Implications for the 2008 Great Wenchuan earthquake. Tectonophysics 491, 154–164.
Wang, K., Shen, Z.K., 2011. Location and focal mechanism of the 1933 Diexi earthquake and its associated regional tectonics. Acta Seismol. Sin. 33 (5), 557–567.
Wang, M., 2009. Analysis of GPS data with high precision and study on present-day crustal deformation in China Doctoral dissertation. Institute of Geology, China Earthquake Administration.
Wang, M., Shen, Z.K., Niu, Z.J., Zhang, Z.S., Sun, H.R., Gan, W.J., Wang, Q., Ren, Q., 2003b. Contemporary crustal deformation of the Chinese continent and tectonic block model. Sci. China (Ser. D) 6 (Suppl.), 25–40.
Wang, Q., Zhang, P.Z., Freymueller, J.T., Bilham, R., Larson, K.M., Lai, X.A., You, X.Z., Niu, Z.J., Wu, J.C., Li, Y.X., Liu, J.N., Yang, Z.Q., Chen, Q.Z., 2001. Present-day crustal deformation in China constrained by Global Positioning System measurements. Science 294 (5542), 574–577.
Wang, S., Jiang, Z.S., Zhang, X., Chen, W.S., 2002. Current tectonic deformation and seismogenic characteristics along the northeast margin of Qinghia-Xizang block. Acta Seismol. Sin. 24 (1), 27–34.
Wang, S., Gao, A., Xu, Z., Zhang, X., Guo, Y., 2000. Relocation of earthquakes in northeastern region of Qinghai-Xizang plateau and characteristics of earthquake activity. Acta Seismol. Sin. 13, 257. http://dx.doi.org/10.1007/s11589-000-0034-7.
Wang, Y., 2001. Heat flow pattern and lateral variations of the lithosphere strength in China mainland: constraints on active deformation. Phys. Earth Planet. Int. 126, 121–146.
Wang, Y.Z., Wang, E.N., Shen, Z.K., Wang, M., Gan, W.J., Qiao, X.J., Meng, G.J., Li, T.M., Tao, W., Yang, Y.L., Cheng, J., Li, P., 2008. GPS-constrained inversion of present-day slip rats along major faults of the Sichuan-Yunnan region, China. Sci. China (Ser. D) 51 (9), 1267–1283.
Wang, Y., Wang, M., Shen, Z.-K., Ge, W., Wang, K., Wang, F., Sun, J., 2013. Interseismic deformation field of the Ganzi-Yushu fault before the 2010 Mw 6.9 Yushu earthquake. Tectonophysics 584, 138–143.
Ward, S.N., 1994. A multidisciplinary approach to seismic hazard in southern California. Bull. Seismol. Soc. Am. 84 (5), 1293–1309.
Webb, T.H., Anderson, H., 1998. Focal mechanisms of large earthquakes in the North Island of New Zealand: slip partitioning at an oblique active margin. Geophys. J. Int. 134 (1), 40–86.
Wei, W., Unsworth, M., Jones, A., Booker, J., Tan, H., Nelson, D., Chen, L., Li, S., Solon, K., Bedrosian, P., Jin, S., Deng, M., Ledo, J., Kay, D., Roberts, B., 2001. Detection of widespread fluids in the Tibetan crust by magnetotelluric studies. Science 292 (5517), 716–719.
Wen, X.Z., Xu, X.W., Zheng, R.Z., Xie, Y.Q., Wan, C., 2003. Averaged slip rate and ruptures of modern strong earthquakes along the Ganzi-Yushu fault. Sci. China (Ser. D) 33 (Suppl.), 199–208.
Working Group on California Earthquake Probabilities, 1995. Seismic hazards in southern California: probable earthquakes, 1994–2024. Bull. Seismol. Soc. Am. 85, 379–439.
Wu, J.P., Ming, Y.H., Wang, C.Y., 2006. Regional waveform inversion for crustal and upper mantle velocity structure below Chuandian region. Chin. J. Geophys. 49 (5), 1369–1376.
Xin, H., Liu, M., Zhang, Y., Zeng, X., Hu, Z., 2010. Relocation of the earthquakes in the southeast area of Gansu. J. Seismol. Res. 33 (3), 292–299.
Xu, X.W., Wen, X.Z., Zheng, R.Z., Ma, W.T., Song, F.M., Yu, G.H., 2003a. Present-day tectonic deformation pattern of active blocks in Sichuan-Yunnan region and its dynamics. Sci. China (Ser. D) 33 (Suppl.), 151–162.
Xu, X., Tapponnier, P., Van der Woerd, J., Ryerson, F.J., Wang, F., Zheng, R.Z., Chen, W. B., Ma, W.T., Yu, G.H., Chen, G.H., Mériaux, A.S., 2003b. Left slip rate across the Altyn tagh fault during late Quaternary and discussions on transition model of tectonic movement. Sci. China (Ser. D) 33 (10), 967–974.
Yang, Z., Chen, Y., Zheng, Y., Yu, X., 2003. Accurate relocation of earthquakes in central-western China using the double-difference earthquake location algorithm. Sci. China 46 (S2), 181–188.
Yang, Z., Yu, X., Zheng, Y., Chen, Y., Ni, X., Chan, W., 2004. Earthquake relocation and three-dimensional crustal structure of P-wave velocity in central-western China. Acta Seismol. Sin. 26 (1), 19–29.
Yao, H., van der Hilst, R.D., Montagner, J.-P., 2010. Heterogeneity and anisotropy of the lithosphere of SE Tibet from surface wave array tomography. J. Geophys. Res. 115 (B12307). http://dx.doi.org/10.1029/2009JB007142.
Yuan, D.Y., Zhang, P.Z., Liu, X.L., Liu, B.C., Zheng, W.J., He, W.G., 2004. The tectonic activity and deformation features during the late Quaternary of Elashan Mountain active fault zone in Qinghai province and its implication of the deformation of the northeastern margins of the Qinghai-Tibet Plateau. Earth Sci. Front. 11 (4), 393–402.
Zhang, K.L., Wei, D.P., 2011. Implications from the kinematic pattern of the Longmenshan region. Tectonophysics 504, 57–64.
Zhang, P.Z., Shen, Z.K., Wang, M., Gan, W.J., Bürgmann, R., Molnar, P., Wang, Q., Niu, Z.J., Sun, J.Z., Wu, J.C., Sun, H.R., You, X.Z., 2004. Continuous deformation of the Tibetan Plateau from global positioning system data. Geology 32 (9), 809–812.
Zhang, X.L., Jiang, Z.S., Chen, B., Li, H., 2002. Preliminary research on present block demarcation, movement and deformation in northeast margin of Qinghai-Tibet. J. Geodesy Geodyn. 22 (1), 63–67.
Zhao, J.R., Li, S.L., Zhang, X.K., Yang, Z.X., Zhang, C.K., Liu, B.F., Zhang, J.S., Pan, S.Z., 2005. Three dimensional Moho geometry beneath the northeast edge of the Qinghai-Tibet Plateau. Chin. J. Geophys. 48 (1), 78–85.
Zhou, D.M., Gan, W.J., Ren, J.W., Ni, G.H., Ning, S.Z., 2005. Inversion of slip rates of the Zhuanglanghe faults and the northern marginal fault of Maxianshan based on GPS measurements. Seismol. Geol. 27 (4), 706–714.
Zhu, A., Xu, X., Yu, G., Zhang, X., Chen, G., Ren, Y., 2012. Relocation of the Yushu Ms 7.1 earthquake sequence and investigation on its seismotectonics. Earth Sci. Front. 19 (4), 008–014.

Yanzhao Wang
Associate researcher, Institute of Geology, China Earthquake Administration.
Ph. D. in Geophysics, 2009, Institute of Geology, China Earthquake Administration.

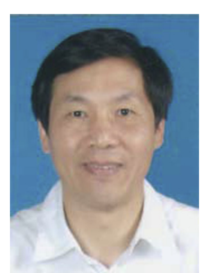

Zheng-Kang Shen
Professor, Peking University.
Ph.D. in Geophysics and Space Physics, 1991, UCLA.

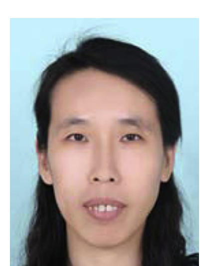

Min Wang
Researcher, Institute of Geology, China Earthquake Administration.